The Astrophysical Journal, 749:135 (19pp), 2012 April 20 doi:10.1088/0004-637X/749/2/135

A NEW IMPLEMENTATION OF THE MAGNETOHYDRODYNAMICS-RELAXATION METHOD FOR NONLINEAR FORCE-FREE FIELD EXTRAPOLATION IN THE SOLAR CORONA

Chaowei Jiang and Xueshang Feng
SIGMA Weather Group, State Key Laboratory for Space Weather, Center for Space Science and Applied Research, Chinese Academy of Sciences, Beijing 100190, China; cwjiang@spaceweather.ac.cn, fengx@spaceweather.ac.cn

Received 2011 December 16; accepted 2012 January 30; published 2012 April 2

ABSTRACT

The magnetic field in the solar corona is usually extrapolated from a photospheric vector magnetogram using a nonlinear force-free field (NLFFF) model. NLFFF extrapolation needs considerable effort to be devoted to its numerical realization. In this paper, we present a new implementation of the magnetohydrodynamics (MHD) relaxation method for NLFFF extrapolation. The magnetofrictional approach, which is introduced for speeding the relaxation of the MHD system, is realized for the first time by the spacetime conservation-element and solution-element scheme. A magnetic field splitting method is used to further improve the computational accuracy. The bottom boundary condition is prescribed by incrementally changing the transverse field to match the magnetogram, and all other artificial boundaries of the computational box are simply fixed. We examine the code using two types of NLFFF benchmark tests, the Low & Lou semi-analytic force-free solutions and a more realistic solar-like case constructed by van Ballegooijen et al. The results show that our implementation is successful and versatile for extrapolations of either the relatively simple cases or the rather complex cases that need significant rebuilding of the magnetic topology, e.g., a flux rope. We also compute a suite of metrics to quantitatively analyze the results and demonstrate that the performance of our code in extrapolation accuracy basically reaches the same level of the present best-performing code, i.e., that developed by Wiegelmann.

Key words: magnetic fields – magnetohydrodynamics (MHD) – methods: numerical – Sun: corona

Online-only material: color figures

1. INTRODUCTION

The magnetic field's configuration is essential for us to understand solar explosive phenomena such as flares and coronal mass ejections. In addition, the magnetic field also plays a crucial role in determining the slowly evolving structures of the solar corona such as the coronal streamers and the coronal holes. However, direct measurements of these magnetic fields are very difficult to implement, and the present observations for the magnetic fields based on the spectropolarimetric method (the Zeeman and the Hanle effects) are basically restricted to the visible surface layer, i.e., the photosphere. Even a routine recording of the full surface fields on the photosphere is only available for the line-of-sight (LoS) component (e.g., the daily disk magnetogram provided by the *Solar and Heliospheric Observatory* (*SOHO*) Michelson Doppler Imager). Most of the vector magnetograms at present are locally recorded for active regions and some of them may be unreliable because of large random errors and the 180° ambiguity. Hence, in view of these limitations, researchers resort to using physical models to extrapolate (or reconstruct) the coronal fields from the observable photospheric magnetogram (Sakurai 1989; Aly 1989; Amari et al. 1997; McClymont et al. 1997; Aschwanden 2005; Wiegelmann 2008).

On a large scale with relatively low resolution, the corona fields are usually extrapolated from the LoS magnetogram with models, including the potential field source surface model (Altschuler & Newkirk 1969; Hoeksema 1984) and the magnetohydrodynamic (MHD) models (Mikić et al. 1999; Linker et al. 1999; Feng et al. 2007, 2010). With these models and the global map of photospheric field, i.e., the synoptic map, the extrapolated global fields can be used to study the general structures of the corona and the heliosphere (e.g., the locations, shapes and sizes of coronal holes, coronal streamers, and heliospheric current sheet, and their evolution). On a local scale with high resolution, when one's interest is focused on the active regions, the most common and powerful way of reconstructing the magnetic fields is the nonlinear force-free field (NLFFF) extrapolation from the vector magnetogram. The force-free assumption is a good approximation for fields in the low corona but above the photosphere. This is because, in most parts of the low corona, particularly the strongly magnetized active regions, the plasma β (the ratio of gas pressure p to magnetic pressure $B^2/(2\mu_0)$, i.e., $\beta = 2\mu_0 p/B^2$) is extremely low ($\beta \ll 1$) and the plasma velocity v is also low compared with the Alfvén speed v_A ($v \ll v_A$), which means that the pressure gradient, gravity, and inertial force can be neglected from the momentum equation; thus, the only surviving Lorentz force must be self-balanced, i.e., $\mathbf{j} \times \mathbf{B} = \mathbf{0}$ (where $\mathbf{j}$ is the electric current density and $\mathbf{B}$ is the magnetic field). This means that $\nabla \times \mathbf{B} = \alpha \mathbf{B}$, where the scalar α is the force-free parameter. Generally, α varies spatially for the NLFFF and some popular simplifications include $\alpha = 0$ for a potential field and $\alpha =$ constant for a linear force-free field.

The reasons why the nonlinear force-free model is superior to other much simpler force-free models for the active regions, i.e., the potential field and the linear force-free field models, are mainly as follows (Wiegelmann 2008): (1) observation shows that there are significant nonpotential fields in the active regions, which exclude the potential model; (2) usually the force-free parameter α is a very space-dependent function as derived from the measured vector magnetogram and is also demonstrated by a great contradiction of the observed loops and linear force-free extrapolations; and (3) potential and linear force-free fields are too simple to accurately estimate the free magnetic energy and magnetic topology. On the other hand, one may wonder why the more realistic model, the MHD model (e.g., Wu et al. 2006, 2009), is less commonly used than the NLFFF model. The reason is twofold. First, there is a lack of observed information for gas parameters such as the surface plasma density and velocity, which are critical boundary conditions for the full MHD simulations (Abbett & Fisher 2003; Abbett et al. 2004; Welsch et al. 2004; Wang et al. 2011); second, the numerical realization of a full MHD simulation is greatly limited by the present computational capability. For instance, the Courant–Friedrichs–Lewy (CFL) condition puts rather severe restrictions on the size of the time step for most explicit schemes because densities in the corona are very low while magnetic field strengths in active regions can be quite high (∼kG); this inescapably results in an extremely high Alfvén speed (Abbett & Fisher 2003). The computational limitation of a full MHD especially arises when it is applied to very high resolution and the large-field-view magnetograms currently available.

A variety of numerical codes with different methods have been proposed to implement the NLFFF extrapolations up to the present. The underlying methods of these codes can be classified into six types, including (1) the Grad–Rubin method (Grad & Rubin 1958; Sakurai 1981; Amari et al. 1999, 2006; Wheatland 2004, 2006); (2) the upward integration method (Nakagawa 1974; Wu et al. 1990; Song et al. 2006); (3) the MHD-relaxation method (Chodura & Schlueter 1981; Yang et al. 1986; Mikic & McClymont 1994; Roumeliotis 1996; Valori et al. 2005, 2007; Jiang et al. 2011; Inoue et al. 2011); (4) the optimization approach (Wheatland et al. 2000; Wiegelmann 2004, 2007; Inhester & Wiegelmann 2006; Wiegelmann & Neukirch 2006); (5) the boundary-element method (Yan & Sakurai 2000; Yan & Li 2006; He & Wang 2008; He et al. 2011); and (6) the most recently developed force-free electrodynamics method (Contopoulos et al. 2011). The reader is referred to Wiegelmann (2008) for a comprehensive review of many of these methods. In addition to the difference in methods, the specific realizations (i.e., the codes) differ significantly in many other aspects from software to hardware, e.g., the mesh configuration, the numerical scheme and boundary conditions, the language of the code (i.e., IDL, C, or Fortran), the hardware architecture, and the degree of parallelization. As a consequence, these codes have very different computational speeds and extrapolation accuracies from each other. Schrijver et al. (2006) and Metcalf et al. (2008) have carried out detailed comparisons of some representative codes using the semi-analytic Low & Lou's force-free solutions (Low & Lou 1990) and a Sun-like test case constructed by van Ballegooijen et al. (2007), respectively. They show that, although all the tested codes can achieve the reference solutions qualitatively, the differences by quantity are considerable. Their analysis points out that the implementation of the method plays the same important role as its underlying approach for causing such differences. In particular, they found that the optimization method coded by Wiegelmann (2004) is the fastest converging and the best-performing algorithm.

In our previous work (Jiang et al. 2011), we used a full-MHD-relaxation method for reconstructing the corona field based on our conservation-element and solution-element (CESE)-MHD code (Feng et al. 2007; Jiang et al. 2010). We included both the gravity and gas pressure of plasma in the model for a more realistic emulation of the low corona. The relaxation is solely dependent on a relatively small viscosity term $\nabla \cdot (\nu\rho\nabla\mathbf{v})$ (where ρ and $\mathbf{v}$ are the plasma density and velocity, respectively, and ν is the viscosity) as done by (Mikic & McClymont 1994). It was demonstrated that the MHD-relaxation method, combined with the established CESE-MHD code, can have many advantages over other approaches, such as the simplicity of the implementation, the high accuracy of the computation, and the efficiency of the highly parallelized code. By using the Low & Lou's force-free benchmark, it was also found that our implementation reconstructed a result comparable to the best one by Wiegelmann (2004) reported in Schrijver et al. (2006), which encouraged us to further the work of our method for more realistic applications. It also proved that the force-free model is a good assumption since we start directly from the full MHD and finally reach a very force-free state. Recently, however, in the experiment with the realistic magnetogram, we found that the system is prone to produce very large velocity (of several v_A) when performed on magnetograms with a rather large gradient, which is ordinary in realistic photospheric data. This is because the discretization errors of the large-gradient regions can cause large Lorentz forces, whereas the used viscosity ν is too small to effectively control the motion driven by these forces. Thus, this velocity severely restricts the time step and further decreases the relaxation speed of the entire system. On the other hand, increasing the viscosity may be useful for restricting the plasma velocity, though it also significantly restricts the time step because the CFL condition is

$$\Delta t < 0.5\frac{\Delta x^2}{\nu}, \tag{1}$$

where Δx and Δt are the mesh spacing in space and time, respectively. A time step that is too small is particularly unfavorable for the CESE scheme, which can produce excessive numerical diffusion and lose accuracy (Chang 2002; Feng et al. 2010). Although dealing with this viscosity term can remarkably remedy this problem, the cost is a huge complication of the numerical scheme and parallelization. Moreover, for the case of force-free extrapolation in which only the magnetic field is solved, it obviously gives no payoff when considering the computational restrictions of the full MHD model, e.g., the slow evolution of the weak field and the additional computational resources consumed by solving plasma density and pressure.

In this paper, we propose a new implementation of the MHD-relaxation method for NLFFF extrapolation to avoid the above shortcomings of our previous method. We now adopt the magnetofrictional approach as used by Roumeliotis (1996) and Valori et al. (2007), which explicitly introduces a frictional-like force $\mathbf{F} = -\nu\mathbf{v}$ to the momentum equation. By adjusting the frictional parameter ν, one can control the relaxation of the system more efficiently than by using the viscosity. Different from the convectional form of the magnetofrictional equation as used in Roumeliotis (1996), van Ballegooijen et al. (2000), and Valori et al. (2007), which cannot be solved by many modern computational fluid dynamics or MHD solvers designed for the standard partial differential equation system such as

$$\frac{\partial\mathbf{U}}{\partial t} + \frac{\partial\mathbf{F}}{\partial x} + \frac{\partial\mathbf{G}}{\partial y} + \frac{\partial\mathbf{H}}{\partial z} = \mathbf{S}, \tag{2}$$

we use a form with the time-dependent term of momentum reserved. We show that, through such modification, the equation system can still be written in standard conservation form with source terms, for which the CESE-MHD method is designed. This paper also focuses on a comprehensive examination of the implementation by applying the code to extrapolations of the semi-analytic force-free solutions adopted by Schrijver et al. (2006, hereafter referred to as Paper I) and the more stringent solar-like test used by Metcalf et al. (2008, hereafter referred to as Paper II). All these tests will be carried out with the same conditions as much as possible (i.e., the same mesh resolution, the same initial potential field, and the same artificial boundary conditions), as in the above two papers, in order to perform a rigid assessment and comparison with the results reported there. We will show that, through this new implementation, we successfully improved our method over the previous work of Jiang et al. (2011). Quantitative comparisons of the results will demonstrate that our performance of the extrapolation accuracy basically reaches the same level of the present best-performing code by Wiegelmann (2004) even for the rather stringent test cases.

The remainder of the paper is organized as follows. In Section 2, we describe the model equations and the numerical implementation. In Section 3, we give a brief review of the benchmark models used for testing the code. The metrics that are used to evaluate the results of extrapolations are given in Section 4 and the extrapolation results and comparisons are reported and discussed in Section 5. Finally, we offer concluding remarks and some outlooks in Section 6.

2. THE METHOD

2.1. *The Magnetofrictional Equations*

In the magnetofrictional method, an artificial frictional force is introduced to the MHD momentum balance equation:

$$\rho \frac{D\mathbf{v}}{Dt} = \frac{\partial(\rho\mathbf{v})}{\partial t} + \nabla \cdot (\rho\mathbf{v}\mathbf{v}) = -\nabla p + \rho\mathbf{g} + \mathbf{J} \times \mathbf{B} - \nu\mathbf{v}, \quad (3)$$

where current $\mathbf{J} = \nabla \times \mathbf{B}$ and ν is the frictional coefficient. In situations for seeking a force-free field, the plasma pressure and gravity can be neglected, which leads to the following zero-beta equation:

$$\rho \frac{D\mathbf{v}}{Dt} = \mathbf{J} \times \mathbf{B} - \nu\mathbf{v}. \quad (4)$$

By further discarding the inertial term, i.e., $D\mathbf{v}/Dt = \mathbf{0}$, it finally gives the usually adopted form of the magnetofrictional method (van Ballegooijen et al. 2000; Valori et al. 2007),

$$\nu\mathbf{v} = \mathbf{J} \times \mathbf{B}. \quad (5)$$

This is simply a balance between the Lorentz force and the friction term; thus, the velocity can be obtained explicitly in terms of the magnetic field. This velocity from Equation (5) can then be input to the magnetic induction equation:

$$\frac{\partial\mathbf{B}}{\partial t} = \nabla \times (\mathbf{v} \times \mathbf{B}), \quad (6)$$

which drives the evolution of the magnetic field. Note that, with such simplification, the only equation that needs solving is the induction equation. A simple finite-difference method can be used to solve it as long as the frictional coefficient is large enough to suppress the potential numerical instability.

In this paper, we do not use the conventional form of the magnetofrictional equation. To utilize the existing CESE solver, we partially reserve the inertial term in Equation (4). Specifically, the time-dependent form of the momentum equation is retained as follows:

$$\frac{\partial(\rho\mathbf{v})}{\partial t} = (\nabla \times \mathbf{B}) \times \mathbf{B} - \nu\rho\mathbf{v}, \ \ \rho = |\mathbf{B}|^2 + \rho_0, \quad (7)$$

where only the term $\nabla \cdot (\rho\mathbf{v}\mathbf{v})$ is omitted from Equation (4). Here the density ρ is set for a nearly uniform Alfvén speed to roughly equalize the speed of evolution of the entire field, and a small value ρ_0, e.g., $\rho_0 = 0.01$, is necessary to deal with a very weak field associated with the magnetic null. This form is also different from the zero-beta model since the time variation of momentum $\mathbf{p} = \rho\mathbf{v}$ is only locally induced by the Lorentz force and the frictional term, without being affected by the neighboring plasma. This has the benefit of using a rather nonuniform density such as $\rho \propto B^2$.

For the induction equation, we use

$$\frac{\partial\mathbf{B}}{\partial t} = \nabla \times (\mathbf{v} \times \mathbf{B}) - \mathbf{v}\nabla \cdot \mathbf{B} + \nabla(\mu\nabla \cdot \mathbf{B}). \quad (8)$$

The terms $-\mathbf{v}\nabla \cdot \mathbf{B}$ and $\nabla(\mu\nabla \cdot \mathbf{B})$ added to the induction equation are both aimed at controlling the numerical error of $\nabla \cdot \mathbf{B}$. The first term, $-\mathbf{v}\nabla \cdot \mathbf{B}$, is derived from Powell's eight-wave MHD model (Powell et al. 1999) and the second term is a diffusive control of $\nabla \cdot \mathbf{B}$ (Marder 1987; Dedner et al. 2002) with a diffusive coefficient μ. The effect of these control terms can be seen explicitly by taking the divergence of the induction equation:

$$\frac{\partial\rho_m}{\partial t} = -\nabla \cdot (\mathbf{v}\rho_m) + \nabla^2(\mu\rho_m), \ \ \rho_m = \nabla \cdot \mathbf{B}. \quad (9)$$

Equation (9) shows that the numerical magnetic monopoles, ρ_m, once derived (either because of the numerical error or from the boundary conditions), cannot locally accumulate. Instead, they are effectively convected with the velocity of the plasma $\mathbf{v}$, and meanwhile diffused among the computational volume with the speed of μ.

Another modification is made by utilizing the so-called magnetic field splitting form of the MHD equation originated by Tanaka (1994). By dividing the full magnetic field $\mathbf{B}$ into two parts ($\mathbf{B} = \mathbf{B}_0 + \mathbf{B}_1$), an embedded constant field $\mathbf{B}_0$ and a deviation $\mathbf{B}_1$, accuracy can be gained only by solving the deviation. The magnetic splitting form is usually used for the global simulation of the solar wind or its interaction with a magnetized planet such as Earth (Tanaka 1994; Nakamizo et al. 2009; Feng et al. 2010), since a strong "intrinsic" potential magnetic field is present in these cases. In the case of solving a force-free field, a potential field that matches the normal component of the magnetogram can be regarded as $\mathbf{B}_0$, which is only induced by the current system below the bottom (i.e., the photosphere), while the deviation $\mathbf{B}_1$ can be seen as the field only induced by the currents in the extrapolation volume (above the photosphere). Then, the magnetic splitting form of the magnetofrictional method for solving NLFFF reads as in a complete system:

$$\begin{aligned}
&\frac{\partial\rho\mathbf{v}}{\partial t} = (\nabla \times \mathbf{B}_1) \times \mathbf{B} - \nu\rho\mathbf{v}, \\
&\frac{\partial\mathbf{B}_1}{\partial t} = \nabla \times (\mathbf{v} \times \mathbf{B}) + \nabla(\mu\nabla \cdot \mathbf{B}_1) - \mathbf{v}\nabla \cdot \mathbf{B}_1, \\
&\frac{\partial\mathbf{B}_0}{\partial t} = \mathbf{0}, \quad \nabla \times \mathbf{B}_0 = \mathbf{0}, \quad \nabla \cdot \mathbf{B}_0 = 0, \\
&\quad \rho = |\mathbf{B}|^2 + \rho_0, \ \ \mathbf{B} = \mathbf{B}_0 + \mathbf{B}_1.
\end{aligned} \quad (10)$$

A notable advantage of using the above equations is that we can completely avoid the random numerical currents and divergences remaining in the initial potential field that are computed by Green's function method or another numerical realization. It is commonly noted that, in the extrapolation box, the currents are concentrated in the interior of the volume, while the upper and the surrounding regions are dominated by the relatively weak potential field (Schrijver et al. 2008; DeRosa et al. 2009). Thus, the splitting form can retain the accuracy of this field. Other merits of using the splitting equations will be seen in the implementation of a multigrid-type optimization (Section 2.2).

2.2. *Numerical Implementation*

The above equation system (10) can be written in a general conservation form with source terms as follows:

$$\frac{\partial \mathbf{U}}{\partial t} + \frac{\partial \mathbf{F}}{\partial x} + \frac{\partial \mathbf{G}}{\partial y} + \frac{\partial \mathbf{H}}{\partial z} - \frac{\partial \mathbf{F}_\nu}{\partial x} - \frac{\partial \mathbf{G}_\nu}{\partial y} - \frac{\partial \mathbf{H}_\nu}{\partial z} = \mathbf{S}, \qquad (11)$$

with $\mathbf{U} = (\rho\mathbf{v}, \mathbf{B}_1, \mathbf{B}_0)$; other terms are given in the Appendix. Then, we input these model equations to the CESE code, which is designed for equations that can be written in the standard form mentioned above. The CESE method deals with three-dimensional governing equations in a substantially different way that is unlike traditional numerical methods (e.g., the finite-difference or finite-volume schemes). The key principle, also a conceptual leap of the CESE method, is treating space and time as one entity. By introducing the CESEs as the vehicles for calculating the spacetime flux, the CESE method can enforce conservation laws both locally and globally in their natural spacetime unity form. Compared with many other numerical schemes, the CESE method can achieve higher accuracy with the same mesh resolution and provide simple mathematics and coding free of any type of Riemann solver or eigendecomposition. Thus, it can benefit for the nonhyperbolic system like the present form of magnetofrictional model (10). For more detailed descriptions of the CESE method for MHD simulations, see Feng et al. (2006, 2007), Zhang et al. (2006), and Jiang et al. (2010, 2012).

The initial and boundary conditions are given as usual in the MHD-relaxation method for NLFFF extrapolation (Roumeliotis 1996; Valori et al. 2007; Jiang et al. 2011). The initial magnetic field is supplied with the potential field $\mathbf{B}_{\rm pot}$ computed using the LoS magnetogram. In the magnetic splitting form, it is simply set by $\mathbf{B}_0 = \mathbf{B}_{\rm pot}$ and $\mathbf{B}_1 = \mathbf{0}$. The system is begun from a static state ($\mathbf{v} = \mathbf{0}$) and driven by inputting vector-magnetic information into the bottom boundary. Specifically, at the bottom boundary, the magnetic field $\mathbf{B}_1$ is linearly changed from the initial value $\mathbf{0}$ to the final value $\mathbf{B}_{\rm vec} - \mathbf{B}_{\rm pot}$ ($\mathbf{B}_{\rm vec}$ is the vector magnetogram) in several values of Alfvén time τ_A. In such a process, the Lorentz forces are continuously injected from the bottom to drive the system away from the initial potential field. After that, the bottom boundary is fixed for the system can reach a new equilibrium. During the entire evolution, the lateral and top faces are fixed as $\mathbf{B}_1 = \mathbf{0}$ and the velocity of all boundaries is unchanged as $\mathbf{v} = \mathbf{0}$.

The time step Δt is restricted by the CFL condition as

$$\Delta t = 0.5\frac{\Delta x}{v_A + v_{\rm max}}, \qquad (12)$$

where the Alfvén speed $v_A = 1$ and $v_{\rm max}$ is the maximum velocity of the entire computational domain. In this context, an arbitrary choice of the frictional coefficient ($\nu > 0$) can be workable because the numerical instability is prohibited by the CFL condition. But choosing a proper ν is particularly important since it controls the relaxation speed of the system. A simple half-discretizing of the momentum equation (7) gives

$$\frac{\mathbf{p}^{n+1} - \mathbf{p}^n}{\Delta t} = \mathbf{J} \times \mathbf{B} - \nu\mathbf{p}^{n+1}, \qquad (13)$$

where n denotes the time level (note that the source terms, e.g., the friction, are treated implicitly in the CESE method), and, thus,

$$\mathbf{p}^{n+1} = \frac{\mathbf{p}^n + \Delta t\mathbf{J} \times \mathbf{B}}{1 + \nu\Delta t}. \qquad (14)$$

Equation (14) shows that the effect of the friction is simply to reduce the momentum at every time step by a factor of $1 + \nu\Delta t$. A ν that is too low may lead to a velocity that is too high ($\geqslant v_A$), which may excessively distort the field line. On the other hand, friction that is too strong will suppress the velocity to a very low value that makes the system too difficult to be driven. To compromise, we set $\nu = 4c\Delta t/\Delta x^2$, which gives the factor

$$1 + \nu\Delta t = 1 + \frac{c}{(1 + v_{\rm max})^2}, \qquad (15)$$

where $c \sim 1$ is variable for optimizing the relaxation. In this form, the friction is adaptively optimized for both the driving and relaxing processes according to the maximum velocity: in the driving process, the velocity is relatively large, which reduces the friction for fast evolution away from the initial field; in the relaxing process, the velocity becomes smaller, which will increase the friction for fast relaxation to equilibrium. A similar setting of ν is also done by van Ballegooijen et al. (2000) and Valori et al. (2007). Finally, for the diffusive coefficient of $\nabla \cdot \mathbf{B}$, we set $\mu = 0.4\Delta x^2/\Delta t$ to maximize the diffusive effect without introducing numerical instability.

One great challenge of the NLFFF reconstructions is the limitation of computational resources, especially for the extrapolation of currently available high-resolution and large-field-view magnetograms; thus, a parallel computation is generally required. Our method is parallelized by the AMR-CESE code (Jiang et al. 2010, 2011), which is a combination of the CESE code within the PARAMESH toolkit (an open-source Fortran package for implementing the parallel-AMR technique on existing code; MacNeice et al. 2000) and is performed on a share-memory parallel cluster. Also, for a large magnetogram, a multigrid-like strategy is recommended to accelerate the computation and improve the quality of extrapolation (Metcalf et al. 2008). We serially compute the solution on a number of grids with a resolution ratio of two and input the results of the coarser resolution to initialize the next finer resolution. It should be noted that such a method is not a standard multigrid since it does not incorporate different grids simultaneously or iterate back and forth between coarser and finer grids. Instead, it computes the solution of different grids only once and uses the coarser solution to initialize the finer grid. The main advantage of doing this is to provide a better (than the potential field) starting equilibrium on the full resolution grid. In particular, standard node-centered, full-weighting restriction and prolongation operators of the multigrid method are used to transfer data between different resolutions. Using these operators, any boundary values are interpolated using data on the same boundary face, and the total flux of the magnetogram is conserved between different grids. It is worth noting that, when using the coarser results to initialize the finer grid, the magnetic splitting form can have accuracy because the deviation field $\mathbf{B}_1$ is only needed to interpolate, while the intrinsic potential field $\mathbf{B}_0$ is always reset

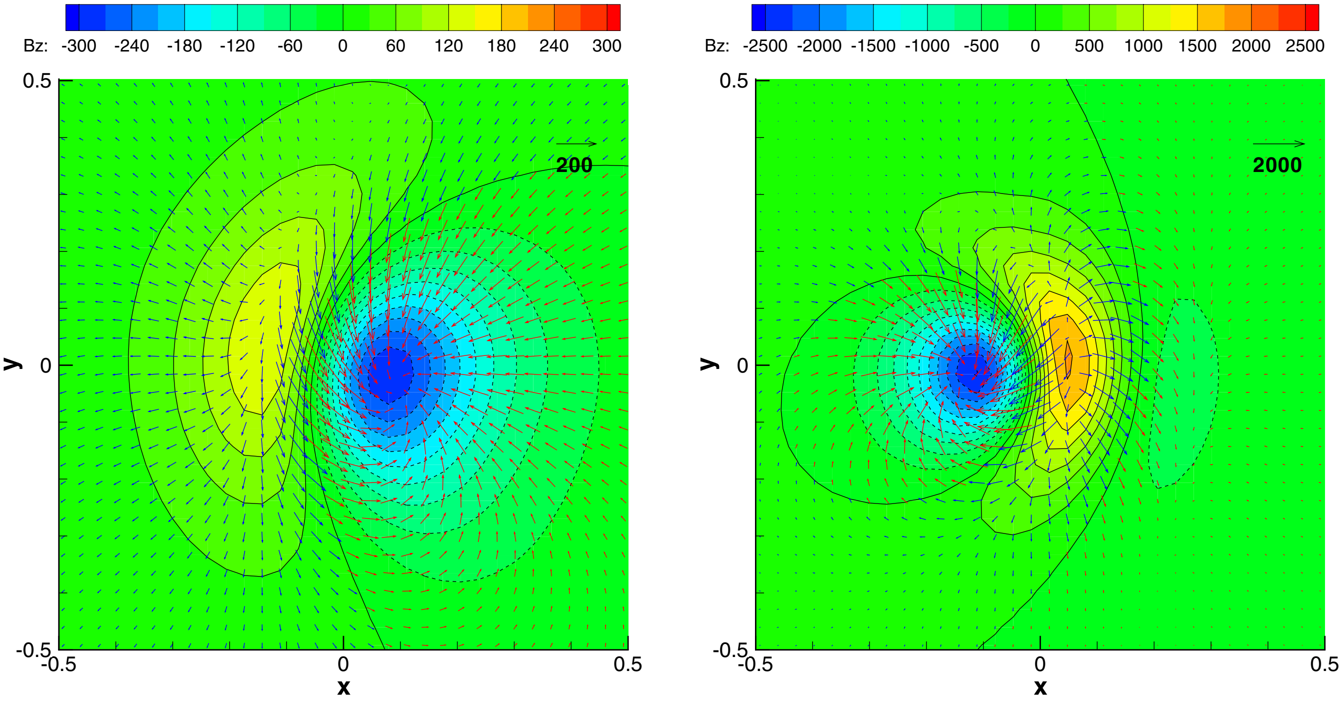

Figure 1. Vector magnetograms of the central region $x, y \in [-0.5, +0.5]$ for CASE LL1 (left) and CASE LL2 (right). The contours represent B_z. The tangential field is shown by the vectors with blue color in the positive B_z region and red in the negative B_z region.

(A color version of this figure is available in the online journal.)

by the value on the final resolution or Green's function method. However, the multigrid algorithm has a shortcoming in that every prolongation (by interpolation) will introduce new errors of divergence and current to $\mathbf{B}_1$ that can be "felt" by the CESE method. Such a problem is also faced in many AMR simulations due to the mesh refinement (Tóth & Roe 2002). We will discuss its effects in Section 5 by comparing the results with and without the multigrid algorithm.

3. BENCHMARK MODELS

3.1. Low & Lou's Force-free Field

The NLFFF model derived by Low & Lou (1990) has served as a standard benchmark for many extrapolation codes (Wheatland et al. 2000; Amari et al. 2006; Schrijver et al. 2006; Valori et al. 2007; He & Wang 2008; Jiang et al. 2011). The fields of this model are basically axially symmetric and can be represented by a second-order ordinary differential equation derived in spherical coordinates:

$$(1-\cos^2\theta)\frac{d^2P}{d(\cos\theta)^2}+n(n+1)P+a^2\frac{1+n}{n}P^{1+2/n}=0, \quad (16)$$

where n and a are constants. Then the magnetic field is given by

$$B_r=\frac{1}{r^2\sin\theta}\frac{\partial A}{\partial\theta}, \quad B_\theta=-\frac{1}{r\sin\theta}\frac{\partial A}{\partial r}, \quad B_\phi=\frac{1}{r\sin\theta}Q, \quad (17)$$

where $A = P(\cos\theta)/r^n$ and $Q = aA^{1+1/n}$. The solution P of Equation (16) is uniquely determined by two eigenvalues, n and its number of nodes m (Low & Lou 1990; Amari et al. 2006). By arbitrarily positioning a plane in the space of the analytical fields, one obtains a different kind of test case in which the plane represents the bottom boundary condition for the extrapolation of the overlaying fields. In this way, the fields sliced by the plane do not show any more symmetry and, thus, benefit a general testing of extrapolation. The position of the plane is characterized by two additional parameters, l and Φ. Here we choose two particular solutions characterized by the parameters $n, m, l,$ and Φ, which are respectively given by $n = 1$, $m = 1$, $l = 0.3$, and $\Phi = \pi/4$ (referred to as CASE LL1), and $n = 3$, $m = 1$, $l = 0.3$, and $\Phi = 4\pi/5$ (CASE LL2). For both cases, the computational domain is $x, y \in [-1, +1]$ and $z \in [0, 2]$ and is discretized by a uniform grid of $64 \times 64 \times 64$ (same as in Paper I). The same test solutions are also used in the above references where more analyses of these fields can be found. The vector magnetograms for both cases at $z = 0$ are shown in Figure 1 and their three-dimensional field lines are shown in panel (a) of Figures 4 and 7. Basically, nonpotential fields occupy more volume in CASE LL1 than in CASE LL2, and CASE LL2 is "more nonlinear" with a larger α and stronger fields more concentrated near the center of the model volume. Since the solutions show rather smooth (small gradients) and relatively simple magnetic structures with their topologies roughly consistent with those of the potential fields based on the same LoS magnetograms, these tests can be regarded as preliminary tests for any newly developed NLFFF extrapolation methods before facing more stringent cases or realistic magnetograms.

3.2. The van Ballegooijen Reference Model

The van Ballegooijen reference model is adopted from Paper II for a more stringent and realistic testing of our code. Using this reference model, it is possible to mimic the analysis of real observational data while still knowing the properties of the field to be modeled. This model field is constructed by initially inserting an S-shaped flux bundle into a potential field associated with active region AR 10814 (see panel (a) of Figure 3), and then relaxing the unbalanced system to a

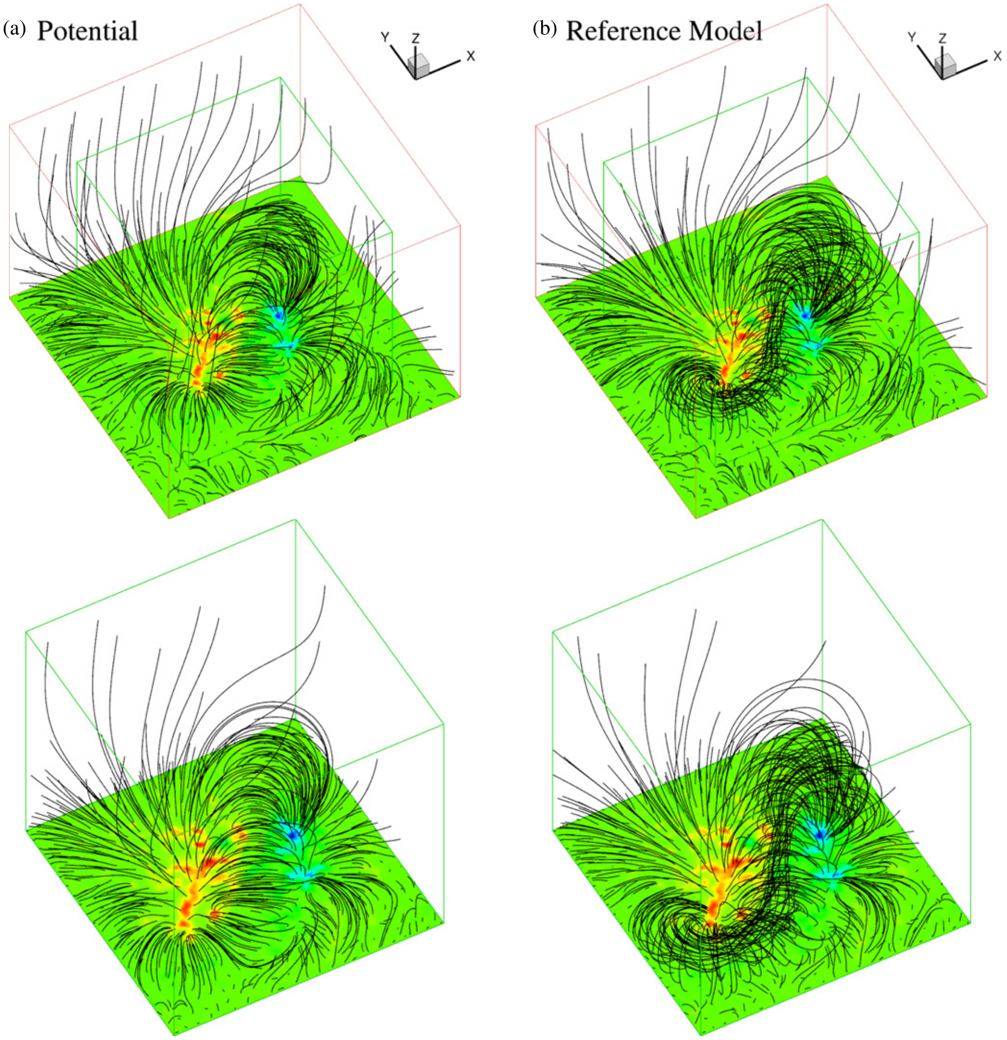

Figure 2. van Ballegooijen reference model: magnetic field lines with a contour of B_z on the bottom surface. The field lines shown are traced from footpoints equally spaced at the bottom surface. (a) The initial potential field and (b) the final near-force-free reference model. The bottom row enlarges the central region outlined by the small cube in the top row.

(A color version of this figure is available in the online journal.)

near-force-free state using van Ballegooijen's magnetofrictional code in spherical geometry (van Ballegooijen et al. 2000; van Ballegooijen 2004). Furthermore, an upward force was applied to the field at the lower boundary during the relaxation process to mimic the effect of magnetic buoyancy in the photosphere, thus achieving more realistic magnetic fields between photospheric and chromospheric heights in the model. Finally, through coordinate transformation and interpolation from the original spherical geometry, magnetic fields in a Cartesian box of 320 × 320 × 258 pixels centered on the active region are extracted as the final reference model. The final near-force-free field is drawn in panel (b) of Figure 3, which contains several interesting topological features, including a coronal null and its associated separatrix surface, and the S-shaped flux bundle surrounded by a quasiseparatrix layer (see more details in Paper II). Compared with the initial potential field, the magnetic topology near the bottom is significantly modified by the low-lying flux rope, which challenges the extrapolation much more than the Low & Lou cases. Because of the extra force presented at the bottom, this reference model can be used for tests of extrapolations from either the "chromospheric" or the "photospheric" magnetograms by providing the NLFFF code with data at $z = z_2$ or $z = z_0$ (z is the height in the model, e.g., z_0 is the base of the reference model). For the "chromospheric" case, the boundary data used are largely force-free, which is consistent with the extrapolation method, while the "photospheric" case is more forced and thus represents a more realistic magnetogram of observation. It should be stressed that the van Ballegooijen reference model is not strictly force-free for the entire model box, even above the chromosphere, due to the implementation of the magnetofrictional method and some other numerical errors. It is demonstrated that, in the model, the residual forces of at least 5% of the magnetic-pressure force are present up to the height of z_{30}, which is consistent with what is known of forces on the Sun. This makes the model a realistic, solar-like test case for the extrapolation codes.

As was done in Paper II, we will test our code using both the chromospheric and the photospheric cases. For the photospheric case, which is inconsistent with force-free assumption, we only examine the code with the photospheric magnetogram preprocessed by the method of Wiegelmann & Neukirch (2006). The magnetograms of both test cases are plotted in Figure 2 and show a significant shearing along the polarity inversion line (PIL).

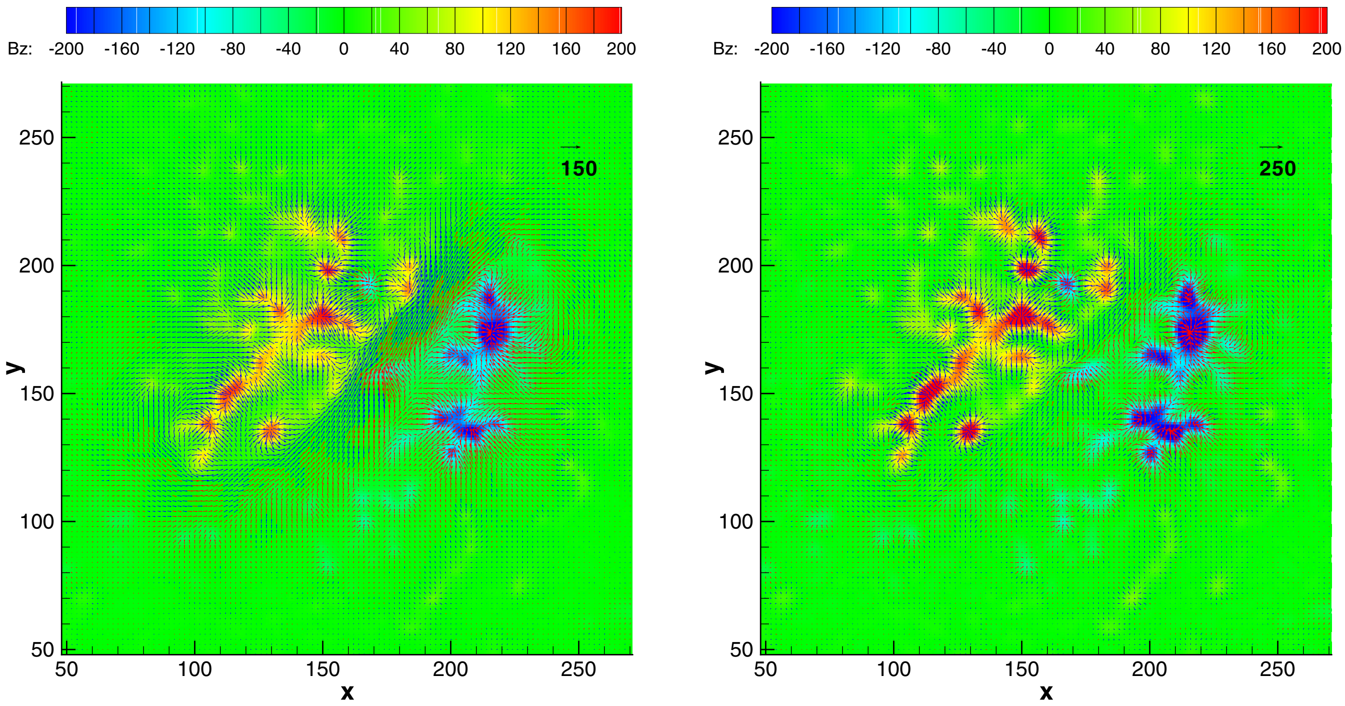

Figure 3. Vector magnetograms of the central 224^2 pixels for the chromospheric case (left) and the preprocessed photospheric case (right). The contours represent B_z with a saturation level of ±200 G. The tangential field is shown by the vectors (plotted at every second grid point) with blue color in the positive B_z region and red in the negative B_z region.

(A color version of this figure is available in the online journal.)

4. METRICS

For a detailed analysis of the extrapolation fields, a suite of metrics introduced in Schrijver et al. (2006) is computed. These metrics compare either local characteristics, including vector magnitudes and directions at each point, or the global energy content. Respectively, they are the vector correlation C_{vec}

$$C_{\mathrm{vec}} \equiv \sum_i \mathbf{B}_i \cdot \mathbf{b}_i \Bigg/ \left(\sum_i |\mathbf{B}_i|^2 \sum_i |\mathbf{b}_i|^2\right), \tag{18}$$

the metric C_{CS} based on the Cauchy–Schwarz inequality

$$C_{\mathrm{CS}} \equiv \frac{1}{M}\sum_i \frac{\mathbf{B}_i \cdot \mathbf{b}_i}{|\mathbf{B}_i||\mathbf{b}_i|}, \tag{19}$$

and the normalized and mean vector error E'_{n}, E'_{m}

$$E_{\mathrm{n}} \equiv \sum_i |\mathbf{b}_i - \mathbf{B}_i| \Bigg/ \sum_i |\mathbf{B}_i|; \quad E'_{\mathrm{n}} = 1 - E_{\mathrm{n}}, \tag{20}$$

$$E_{\mathrm{m}} \equiv \frac{1}{M}\sum_i \frac{|\mathbf{B}_i - \mathbf{b}_i|}{|\mathbf{B}_i|}; \quad E'_{\mathrm{m}} = 1 - E_{\mathrm{m}}, \tag{21}$$

where $\mathbf{B}_i$ and $\mathbf{b}_i$ denote the input field (the Low & Lou's solution or the van Ballegooijen reference model in this paper) and the extrapolated field, respectively, i denotes the indices of the grid points, and M is the total number of grid points involved. As can be seen, an exact extrapolation will contain all the metrics equal to unity in such definitions, and the closer to unity means the better extrapolation and vice versa. Detailed descriptions for these metrics can be found in Amari et al. (2006), Schrijver et al. (2006), and Valori et al. (2007). Another very important parameter for comparing the extrapolation is the free energy of the magnetic field. It is measured by the ratio of extrapolated energy to potential energy using the same magnetogram:

$$E/E_{\mathrm{pot}} = \frac{\sum_i |\mathbf{B}_i|^2}{\sum_i |(\mathbf{B}_{\mathrm{pot}})_i|^2}. \tag{22}$$

It is common to measure the force-freeness and divergence-freeness of the extrapolation using the current-weighted sine metric CWsin and the divergence metric $\langle|f_i|\rangle$ (Metcalf et al. 2008; Schrijver et al. 2008; DeRosa et al. 2009; Canou & Amari 2010), which are defined by Wheatland et al. (2000) as

$$\mathrm{CWsin} \equiv \frac{\sum_i |\mathbf{J}_i|\sigma_i}{\sum_i |\mathbf{J}_i|}; \quad \sigma_i = \frac{|\mathbf{J}_i \times \mathbf{B}_i|}{|\mathbf{J}_i||\mathbf{B}_i|} \tag{23}$$

and

$$\langle|f_i|\rangle = \frac{1}{M}\sum_i \frac{(\nabla \cdot \mathbf{B})_i}{6|\mathbf{B}_i|/\Delta x}, \tag{24}$$

where Δx is the grid spacing. Both of the metrics are normalized, with the former focused on the directional deviation between the currents and the field lines and the latter on the relative value of residual divergence. These two metrics are equal to zero for an exact force-free field; hence, the smaller the metrics, the better the extrapolation.

In addition to the above metrics, we also introduce another pair of metrics to evaluate the degree of convergence toward the divergence-free and force-free state. For the first one, we note that a nonzero $\nabla \cdot \mathbf{B}$ (i.e., the magnetic monopole) introduces an unphysical force to the system, $\mathbf{F} = \mathbf{B}\nabla \cdot \mathbf{B}$, parallel to the field line (Dellar 2001). To evaluate the effect of this unphysical

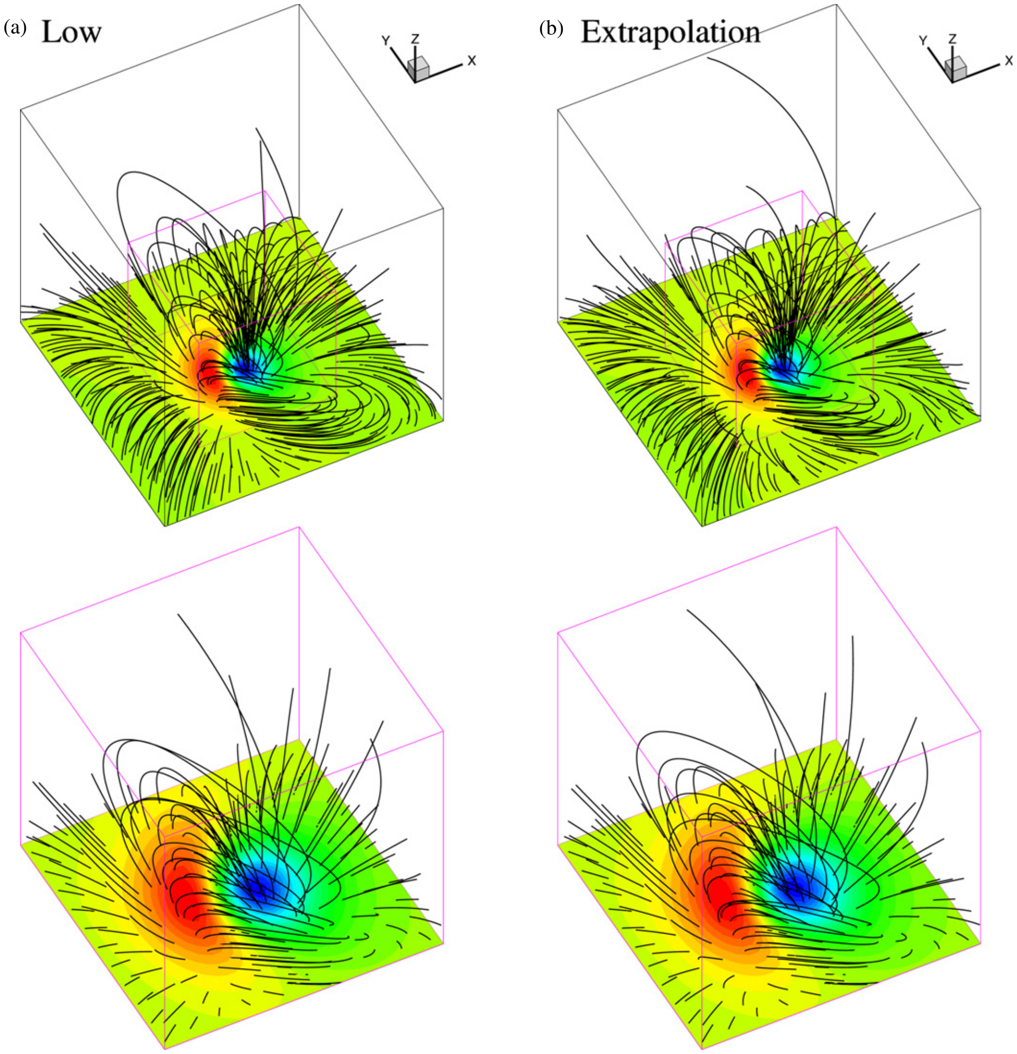

Figure 4. CASE LL1: magnetic field lines with contour of B_z on the bottom surface. (a) The Low & Lou's solution and (b) the extrapolation result. The bottom row enlarges the central region ($x, y \in [-0.5, +0.5]$ and $z \in [0, 1]$) outlined by the small cube in the top row.

(A color version of this figure is available in the online journal.)

force on the numerical computation, the metric $E_{\nabla\cdot\mathbf{B}}$ is defined as the average ratio of this force to the magnetic-pressure force:

$$E_{\nabla\cdot\mathbf{B}} = \frac{1}{M}\sum_i \frac{|\mathbf{B}_i(\nabla\cdot\mathbf{B})_i|}{|\nabla(|\mathbf{B}|^2/2)_i|}. \tag{25}$$

Similarly, the second metric $E_{\nabla\times\mathbf{B}}$ measures the effect of the residual Lorentz force in the same way:

$$E_{\nabla\times\mathbf{B}} = \frac{1}{M}\sum_i \frac{|\mathbf{J}_i\times\mathbf{B}_i|}{|\nabla(|\mathbf{B}|^2/2)_i|}. \tag{26}$$

Unlike the metrics of CWsin and $\langle|f_i|\rangle$, which mainly characterize the geometric properties of the field, these two metrics directly measure the physical action of the residual divergence and Lorentz force on the system in the actual numerical computation. This is important when checking the NLFFF solution if it is used to initiate any MHD simulations.

For the all metrics above, the first four are more rigid since they are involved without any type of derivatives, but the other metrics may be unreliable for comparison with results from different papers due to the specific numerical realization of the derivatives (for example, different orders of numerical differentiation or different configurations of computational grid, e.g., cell-centered or staggered). In the present work, the second-order central difference is used for evaluating all the derivatives associated with the divergence, curl, and gradient operators, although the spatial derivatives can be directly obtained from the CESE method.

5. RESULTS

In this section, we present the results of the extrapolation for the benchmark models. The results are also compared with some results reported in Papers I, II, and Valori et al. (2007).

5.1. Low & Lou's Force-free Field

5.1.1. CASE LL1

Results for CASE LL1 are given in Figures 4 and 5 and Tables 1 and 2. In Figure 4, we show the same selected field lines in a three-dimensional view for the extrapolation results and the reference solution, which are traced from footpoints evenly rooted at the lower boundary. In the central region of core fields (i.e., $x, y \in [-0.5, +0.5]$ and $z \in [0, 1]$, enlarged in the bottom row of the figures), the MHD result is in very good agreement

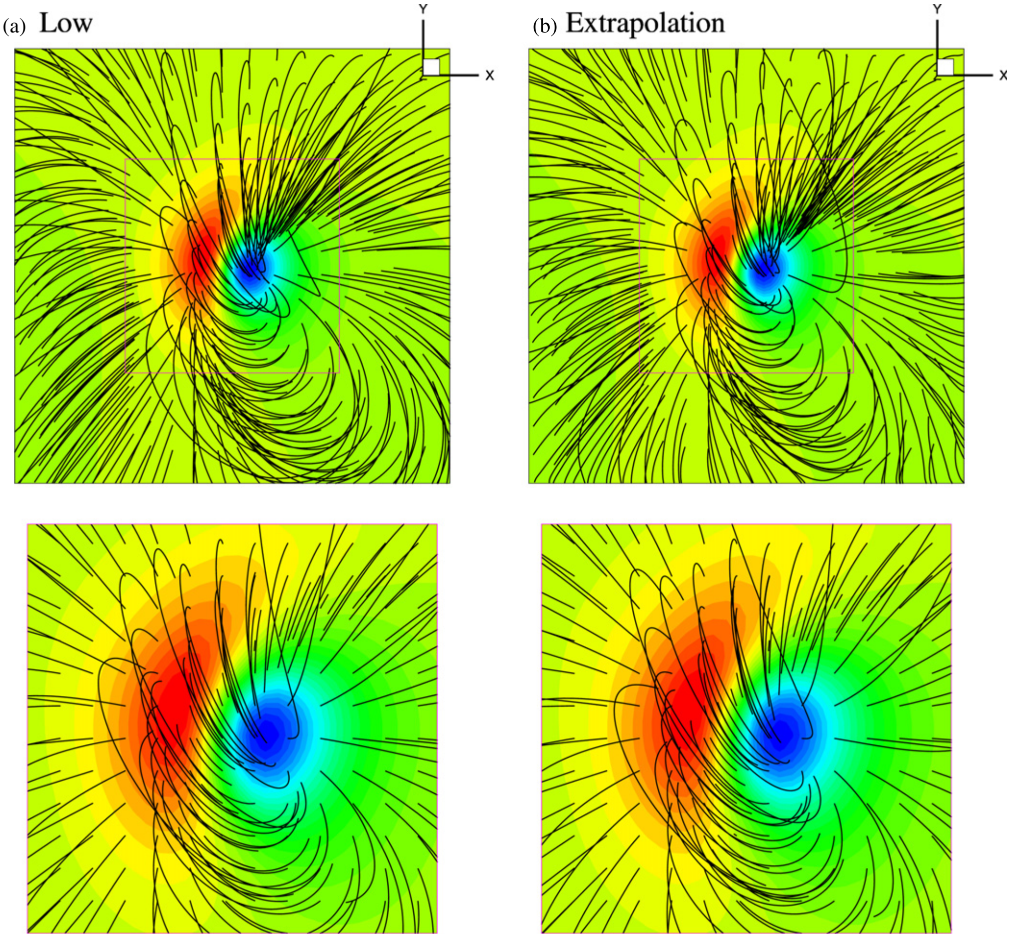

Figure 5. CASE LL1: same as Figure 4, but projected onto the x–y planes.
(A color version of this figure is available in the online journal.)

Table 1
CASE LL1: Metrics for the Central and Entire Regions

Model	$C_{\rm vec}$	$C_{\rm CS}$	$E'_{\rm n}$	$E'_{\rm m}$	$E/E_{\rm pot}$	CWsin	$\langle\lvert f_i\rvert\rangle$
For the central region							
Low	1.000	1.000	1.000	1.000	1.242	0.014	0.94×10^{-4}
Our result	1.000	0.997	0.964	0.912	1.241	0.015	1.67×10^{-4}
Wiegelmann*	1.00	1.00	0.97	0.96	1.26		
Valori**	0.999	0.99	0.95	0.87	1.23	0.009	
Potential	0.858	0.869	0.498	0.443	1.000		
For the entire domain							
Low	1.000	1.000	1.000	1.000	1.294	0.014	0.56×10^{-4}
Our result	0.998	0.955	0.873	0.662	1.282	0.060	1.31×10^{-4}
Wiegelmann*	1.00	1.00	0.98	0.98	1.31	0.070	
Valori**	0.994	0.86	0.80	0.51	1.28	0.019	
Potential	0.852	0.824	0.446	0.353	1.000		

Notes. The superscript "$*$" denotes the reported results in Tables I and II of Paper I, and "$**$" denotes the reported results by Valori et al. (2007).

Table 2
CASE LL1: Metrics of $E_{\nabla\times\mathbf{B}}$ and $E_{\nabla\cdot\mathbf{B}}$

Model	$E_{\nabla\times\mathbf{B}}$	$E_{\nabla\cdot\mathbf{B}}$
For the central region		
Low	0.007	0.005
Our result	0.010	0.008
For the entire region		
Low	0.003	0.002
Our result	0.024	0.005

with Low & Lou's solution, as can be seen from the similarity of most of the field lines. Such agreement is quantitatively demonstrated by the metrics in Table 1. The first three metrics are very close to 1 with an error of <5% and even the most sensitive metric, E'_m, has an error below 10%. In Table 1, we also compare the metrics with the best result by Wiegelmann's code (Wiegelmann 2004) reported in Paper I and extrapolation by Valori et al. (2007). Our result for the central region, although only specifying the lower boundary, still reaches the level of the best extrapolation using information from Low & Lou's solution on all six boundaries. This may be because this test case is close to the potential field, and hence a fixed side and top boundary conditions can rarely impact the central extrapolation. The influence of the boundary conditions is more explicitly shown through a comparison of the metrics for the entire domain. The Wiegelmann's extrapolation still performs perfectly with all four metrics extremely close to unity, while our result and that of Valori et al. perform less exactly, but the results are still satisfactory. Like other results in Table 1, our extrapolation also recovered the energy content very precisely, especially for the central region; furthermore, the metrics evaluating the force-freeness and divergence-freeness are rather small and close to the reference values, which is caused by discretization error. All these results show that extrapolation of a very high accuracy, at

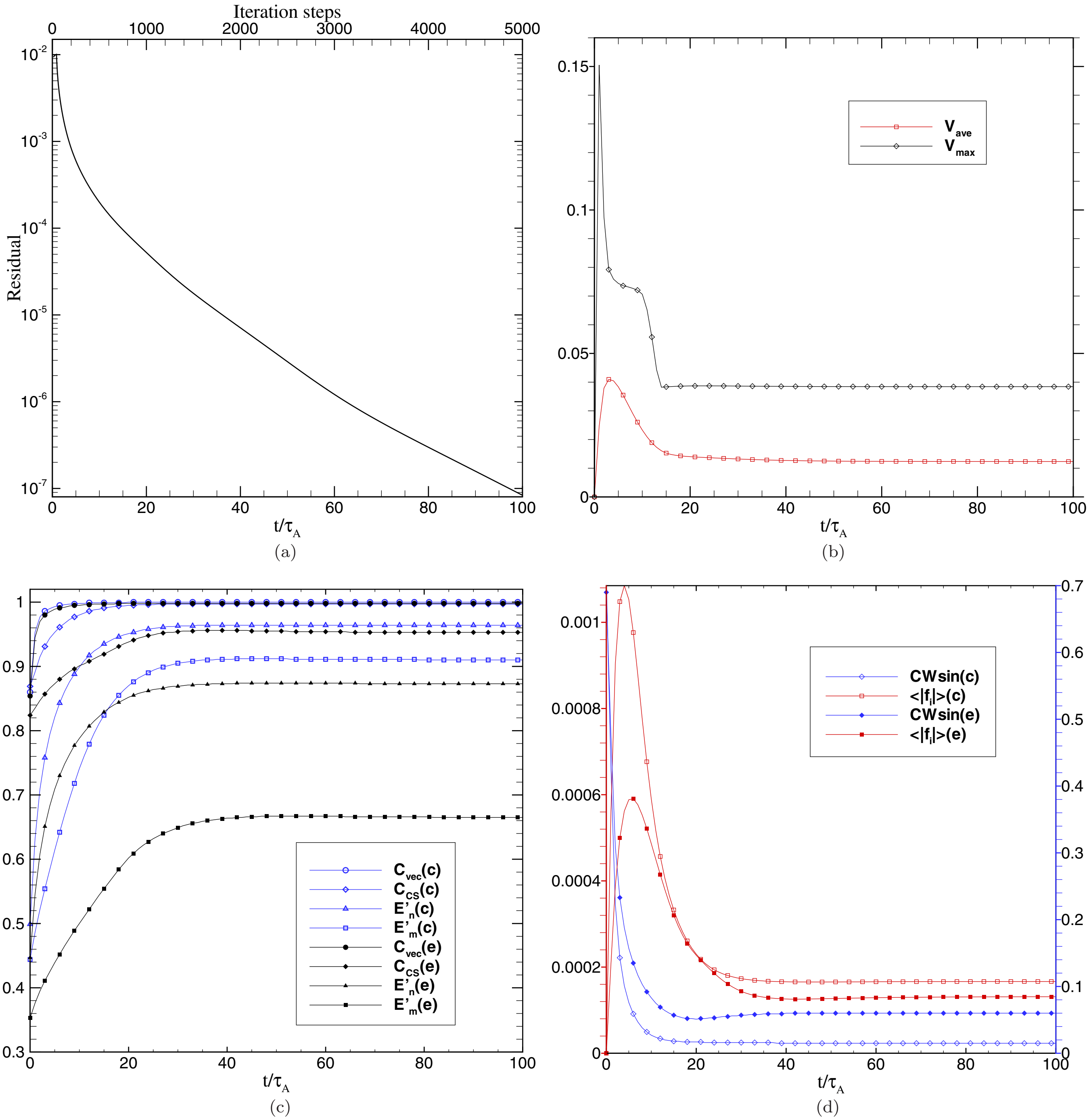

Figure 6. CASE LL1: the history of the relaxation to force-free equilibrium. (a) Evolution of residual res(**B**) with time (or the iteration steps); (b) evolution of the maximum and average velocity; and (c) and (d) evolution of the metrics for the central region (marked by (c)) and the entire volume (marked by (e)).

(A color version of this figure is available in the online journal.)

least for this relatively easy test case, can be achieved using our implementation.

In the Valori's implementation of the magnetofrictional method (Valori et al. 2007), a fourth-order numerical scheme is used with many layers of ghost mesh and a high-order polynomial extrapolation of the fields is adopted on the side and top boundaries. However, by comparing our result with Valori's, it is interesting to note that our implementation performs better, although our numerical scheme is a second-order method without any ghost layers and the boundaries are simply fixed. In this test, the boundary effect can be neglected as mentioned (while in the following test of CASE LL2, we will see the effect of different treatments of these boundaries). Then, we concluded that the better performance is due to the merit of using a better solver, i.e., the CESE method combined with the magnetic splitting algorithm, which can gain additional accuracy.

We finally provide a study of the convergence of the extrapolation. In Figure 6, we show the history of the system relaxing to the final force-free equilibrium, including the residual of

Table 3
CASE LL2: Metrics for the Central and Entire Regions

Model	$C_{\rm vec}$	$C_{\rm CS}$	$E'_{\rm n}$	$E'_{\rm m}$	$E/E_{\rm pot}$	CWsin	$\langle\lvert f_i\rvert\rangle$
For the central region							
Low	1.000	1.000	1.000	1.000	1.099	0.036	3.14×10^{-4}
Our result	0.999	0.933	0.938	0.636	1.114	0.047	7.35×10^{-4}
Wiegelmann*	1.00	0.91	0.92	0.66	1.14		
Valori**	0.999	0.95	0.96	0.75	1.11	0.015	
Potential	0.923	0.661	0.572	0.299	1.000		
For the entire domain							
Low	1.000	1.000	1.000	1.000	1.100	0.035	2.17×10^{-4}
Our result	0.999	0.574	0.852	−1.060	1.115	0.060	6.35×10^{-4}
Wiegelmann*	1.00	0.57	0.86	−0.25	1.14		
Valori**	0.999	0.64	0.88	−0.01	1.11	0.027	
Potential	0.921	0.346	0.465	−0.639	1.000		

Notes. The superscript "∗" denotes the reported results in Tables I and II of Paper I, and "∗∗" denotes the reported results by Valori et al. (2007).

Table 4
CASE LL2: Metrics of $E_{\nabla\times\mathbf{B}}$ and $E_{\nabla\cdot\mathbf{B}}$

Model	$E_{\nabla\times\mathbf{B}}$	$E_{\nabla\cdot\mathbf{B}}$
For the central region		
Low	0.011	0.008
Our result	0.026	0.024
For the entire region		
Low	0.004	0.003
Our result	0.025	0.013

temporal evolution of the magnetic field

$$\mathrm{res}^n(\mathbf{B}) = \sqrt{\frac{1}{3}\sum_{\delta=x,y,z}\frac{\sum_i \left(B^n_{i\delta} - B^{n-1}_{i\delta}\right)^2}{\sum_i \left(B^n_{i\delta}\right)^2}} \qquad (27)$$

(where n denotes the iteration steps), the evolution of the velocity, and the metrics. The system converged very fast from an initial residual of 10^{-2} to value below 10^{-7} with time of $100\tau_A$ (about 5000 iteration steps, see panel (a) of Figure 6). The evolution of the plasma velocity indicates that a static equilibrium is reached as expected with a rather small residual velocity ∼0.01, which is only on the order of the numerical error $O(\Delta x^2)$ of the CESE solver. All the metrics plotted in the figure converged after $40\tau_A$ (about 2000 iteration steps), when the residual is on the order of 10^{-5}. Note that the metric f_i of $\nabla \cdot \mathbf{B}$, like the plasma velocity, first climbs to a relatively high level (∼0.01, see panel (d) of Figure 6) and then drops to the level of discretization errors. In principle, the divergence-free constraint of $\mathbf{B}$ should be fulfilled throughout the evolution, at least close to the level of discretization error. However, an ideally dissipationless induction equation (6) with a divergence-free constraint can preserve the magnetic connectivity, which makes the topology of the magnetic field unchangeable (Wiegelmann 2008) unless a finite resistivity is included to allow the reconnection and changing of the magnetic topology (Roumeliotis 1996). In the present implementation in which no resistivity is included in the induction equation, a break of the $\nabla \cdot \mathbf{B}$ constraint in the initial evolution process (indicated by the climb of metric f_i) can thus produce a change in the magnetic topology (also note that a numerical diffusion can help also topology adjustment).

5.1.2. CASE LL2

Now we present the result of the second test, CASE LL2, which is more difficult than the first one. The results are shown in Figures 7 and 8 and Tables 3 and 4. Compared with CASE LL1, this case has more nonpotential and is more nonlinear with a relatively larger gradient of fields. Even after considering this, our extrapolation still provides a satisfactory result that is as good as the best result in Paper I (see the first four metrics shown and compared in Table 3). It is also quite encouraging that our result for the central region is close to Valori's, which is computed with a fourth-order numerical scheme. Figures 7 and 8 demonstrate qualitatively the consistence with the Low & Lou's reference solution. The energy contents are reproduced very well for both the central region and the entire domain.

By comparing the metrics of the entire domain, we find that our result scores worse than Valori's, especially as shown by $E'_{\rm m}$. The reason for this is twofold. First, a high-order scheme can characterize the large gradient much more accurately than the second-order scheme; thus, the fourth-order scheme by Valori et al. (2007) shows its advantages for this test case with larger gradient than CASE LL1 (the high-order accuracy can also be achieved by mesh refinement other than improving the order of the numerical scheme. As demonstrated in our previous work (Jiang et al. 2011), a refined grid of 128 × 128 × 100 with the CESE scheme gave a much more accurate result, with the most sensitive metric even reaching 0.166). Second, our implementation simply fixed the artificial boundaries (i.e., the lateral and top faces), which obviously makes the system overdetermined. In the present test case, the final field is very nonpotential, hence the boundary values significantly deviate from the initial conditions. A fixed boundary condition will tie the field lines that pass through the boundary, which would otherwise freely cross the boundary since this boundary is a nonexisting interface in the realistic corona. This line-tied condition thus hinders the system from relaxing to a true force-free state. The metric of CWsin clearly demonstrates that the field is less force-free than Valori's result. The boundary effect can be seen visually from some field lines close to the lateral boundaries shown in the figures (e.g., see the distortion of field lines at the lower left coroners of panel (b) in Figures 7 and 8). Also caused by the boundary effect, the field for the entire domain (CWsin = 0.060) is thus less force-free than the central region (CWsin = 0.047). In a full MHD simulation, this boundary effect can be minimized by using so-called nonreflecting boundary conditions based on the characteristic decomposition of the full MHD system (Wu et al. 2001, 2006; Hayashi 2005; Feng et al. 2010; Jiang et al. 2011). However, for the present form of the magnetofrictional equation, the characteristic method is no more valid because of the eigendegeneration of the nonhyperbolic system. In such situation, a natural choice for modeling the nonreflecting boundary is to use linear or high-order extrapolation, just as was done by Valori et al. (2007). Fortunately, field configuration like this Low & Lou case with the entire volume being very nonpotential is not usually found in observed magnetograms. By choosing a model box significantly larger than the core nonpotential region, a simply fixed boundary value of the initial potential field is still sufficient for most extrapolations, for example, test cases in the next section.

Figure 9 shows that the convergence speed is even faster than CASE LL1. The residual of the magnetic field reaches the order of 10^{-7} with only ∼3200 iterations at $60\tau_A$. The evolution speed of the magnetic field is also demonstrated by

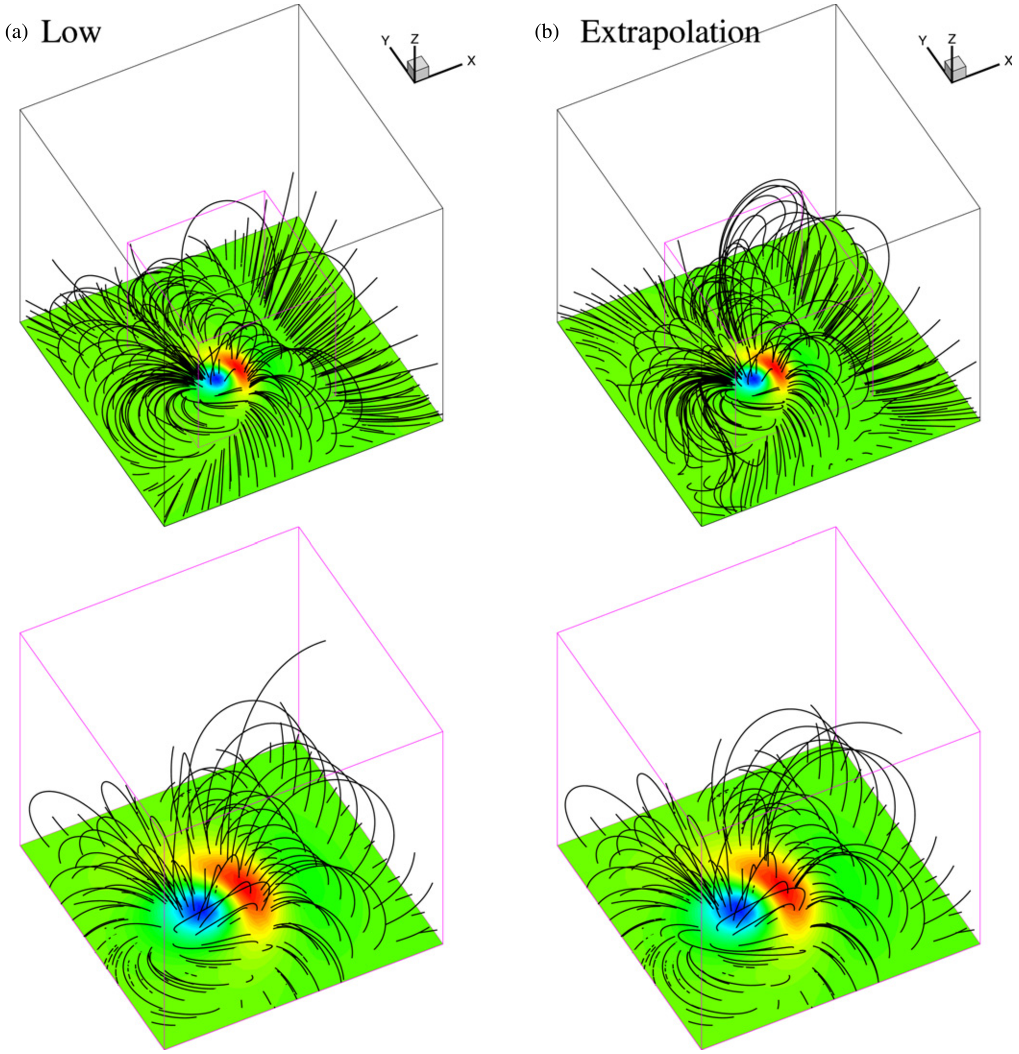

Figure 7. Same as Figure 4 but for CASE LL2.
(A color version of this figure is available in the online journal.)

the magnitude of the plasma velocity, which is larger than that of CASE LL1. At about $30\tau_A$, all the metrics converged with the corresponding residual of the magnetic field on the order of 10^{-5}. This and the preceding cases show that generally the iteration can be stopped when $\mathrm{res}^n(\mathbf{B}) < 10^{-6}$, since after then the temporal change of the magnetic field can actually be neglected.

5.2. The van Ballegooijen Reference Field

We first perform the extrapolation of the chromospheric case, which provides a largely force-free magnetogram without any preprocessing. Figure 10 shows the three-dimensional field lines of extrapolation and the reference model for a side-by-side comparison. The field lines shown are traced from footpoints equally spaced at the bottom surface. We especially adjusted the figures to an orientation that was approximately the same as Paper II to visually compare them with the results from the other codes. The same field lines are also projected on the x–y plane in Figure 11. As shown from an overview of the figures, the extrapolation reproduced quite well the basic magnetic topology, including the low-lying S-shaped field-line bundle and the overlying magnetic arcade that straddles the flux rope. For a confirmation of the presence of the flux rope in the extrapolation, we select a set of field lines of the S-shaped bundle and plot them using different colors in Figure 12 with different perspectives. Figure 12 clearly shows that the flux rope is qualitatively recovered, encouraging us that the code can be used to handle such relatively complex test cases. The extrapolated flux rope is weakly twisted and its core fields basically lie along the bottom PIL, showing a high shear with respect to the overlying arcades.

In Table 5, we give a quantitative evaluation and comparison of the result with those reported in Paper II. To minimize the (side and top) boundary effects, the metrics are applied to the central region of $(x, y) \in [48, 271] \times [48, 271]$ with two different heights: $z \in [2, 61]$ for focusing on the low-lying flux rope and $z \in [2, 225]$ for also including the surrounding potential-like field. This is done in the same way as in Paper II and the results, along with the first three preferable results in Paper II, are presented. Note that some metrics (e.g., the C_{CS} and CWsin) for the reference and potential models differ slightly from those shown in Paper II, which may be due to different precisions (i.e., single or double precision) used in the numerical computation.

As shown in Table 5, the extrapolation performs very well with errors only of ∼2% for the first two metrics. These metrics, however, are not a sensitive indicator of extrapolation accuracy (Valori et al. 2007); thus, all the methods in Paper II

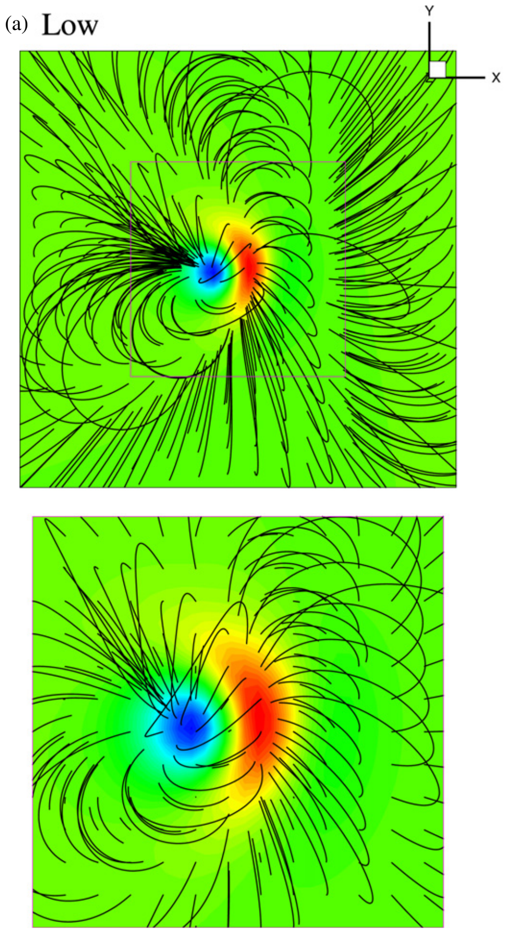

Figure 8. Same as Figure 5 but for CASE LL2.

(A color version of this figure is available in the online journal.)

Table 5

The van Ballegooijen Reference Model: Metrics for Extrapolation of the Chromospheric Case

Model	$C_{\rm vec}$	$C_{\rm CS}$	$E'_{\rm n}$	$E'_{\rm m}$	$E/E_{\rm pot}$	CWsin	$\langle \lvert f_i \rvert \rangle$
For $z \in [2, 225]$							
Reference	1.000	1.000	1.000	1.000	1.343	0.107	1.02×10^{-4}
Our result	0.995	0.978	0.885	0.734	1.337	0.133	1.11×10^{-4}
Our result*	0.993	0.975	0.868	0.712	1.357	0.142	1.32×10^{-4}
Wiegelmann**	1.00	0.99	0.89	0.73	1.34	0.11	
Wheatland**	0.95	0.98	0.79	0.70	1.21	0.15	
Valori**	0.98	0.98	0.84	0.71	1.25	0.15	
Potential	0.852	0.952	0.687	0.665	1.000		
For $z \in [2, 61]$							
Reference	1.000	1.000	1.000	1.000	1.361	0.103	1.33×10^{-4}
Our result	0.995	0.989	0.923	0.883	1.348	0.125	1.58×10^{-4}
Our result*	0.993	0.979	0.902	0.825	1.366	0.129	1.74×10^{-4}
Wiegelmann**	1.00	0.99	0.94	0.89	. . .	0.11	
Wheatland**	0.95	0.95	0.79	0.76	. . .	0.15	
Valori**	0.98	0.96	0.86	0.81	. . .	0.15	
Potential	0.847	0.901	0.660	0.678	1.000		

Notes. The superscript "*" denotes that the multigrid-type algorithm is used to speed up the extrapolation, and the superscript "**" denotes the reported results in Tables 3 and 4 of Paper II.

give these metrics within the same level, even including the potential field. Using the more sensitive metrics $E_{\rm n}$ and $E_{\rm m}$, we find that our result for $z \in [2, 225]$ is identical with the best result performed by Wiegelmann. For the lower height, the deviations of these metrics with the best result are smaller than $<2\%$ (note that these deviations can also be partially introduced by the different precisions in the numerical computation). This comparison encourages us further regarding the success of our implementation. Our result also gives energy metrics very close to the reference values, showing a good recovering of the free-energy content, which is particularly important for coronal field extrapolation. Finally, the CWsin metric behaves a bit worse than the first five metrics when compared with the Wiegelmann's result, but it still scores better than the following results by Wheatland and Valori.

The last two metrics $E_{\nabla\times\mathbf{B}}$ and $E_{\nabla\cdot\mathbf{B}}$ (shown in Table 7), both of which are nonzero but are in a very low level, mean that the reference model is very close to force-free and divergence-free but never exact as expected (see Section 5.2). Again, our results present values very similar to those in the reference model. Note that, although both CWsin and $E_{\nabla\times\mathbf{B}}$ measure the degree of force-free, the former depends more strongly on the high-current regions (Valori et al. 2007) while the latter is not. Hence, CWsin for both heights gives nearly the same value of 0.1, while $E_{\nabla\times\mathbf{B}}$ gives a significantly larger value of 0.06 for the lower domain ($z \in [2, 61]$) than the value of 0.018 for the full domain ($z \in [2, 225]$), which shows that the residual forces are mainly presented in the lower region. Using these two metrics, we demonstrate that our code can minimize the residual forces into a very low value and fulfill the divergence-free condition well.

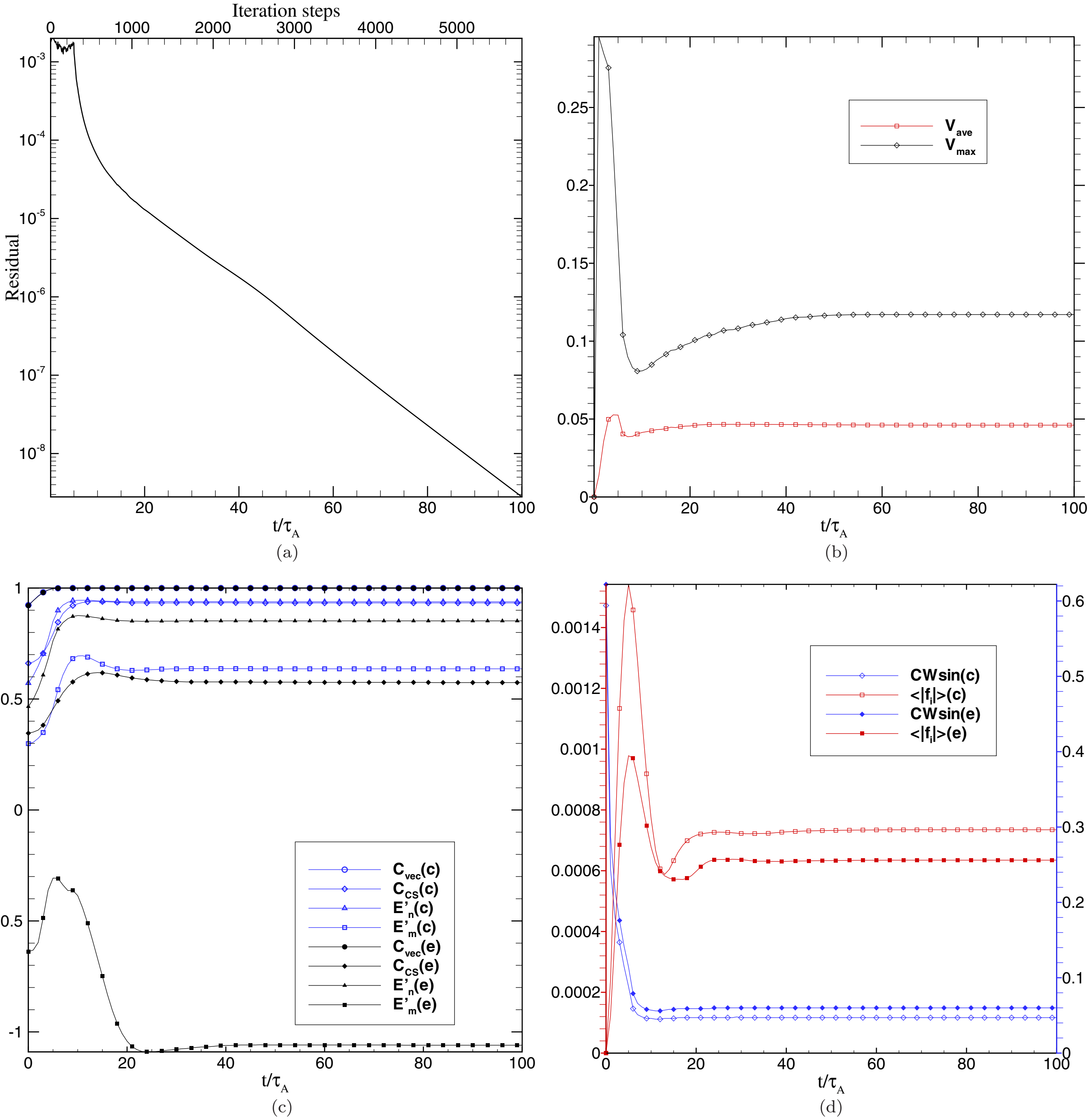

(a) (b) (c) (d)

Figure 9. Same as Figure 6 but for CASE LL2.

(A color version of this figure is available in the online journal.)

In Table 5, the result with the multigrid-type algorithm is also presented, which is performed on a three-grid sequence (80 × 80 × 64, 160 × 160 × 128, and the full resolution 320 × 320 × 256). We found that this result (with a multigrid algorithm) behaves a little bit worse compared with the result without a multigrid algorithm. This is due to the additional numerical errors of $\nabla \times \mathbf{B}$ and $\nabla \cdot \mathbf{B}$ introduced by interpolating the field from a coarser to finer grid, which thus results in a little bit larger value of CWsin and $\langle |f_i| \rangle$ than those without a multigrid algorithm. Without the multigrid algorithm, the magnetic field splitting form can avoid this numerical errors by using a zero $\mathbf{B}_1$ initially and thus performs better. However, in spite of this small disadvantage, the multigrid algorithm is still encouraged to be adopted since its reward is a significant reduction of the computing time (e.g., for the present test case, we find that using the multigrid algorithm saves approximately two-thirds of the CPU time).

Now we present the results for the photospheric case with a preprocessed magnetogram. The preprocessing procedure can remove the net forces of the photospheric magnetogram and hence provide the extrapolation code with a more consistent lower boundary condition than the raw magnetogram.

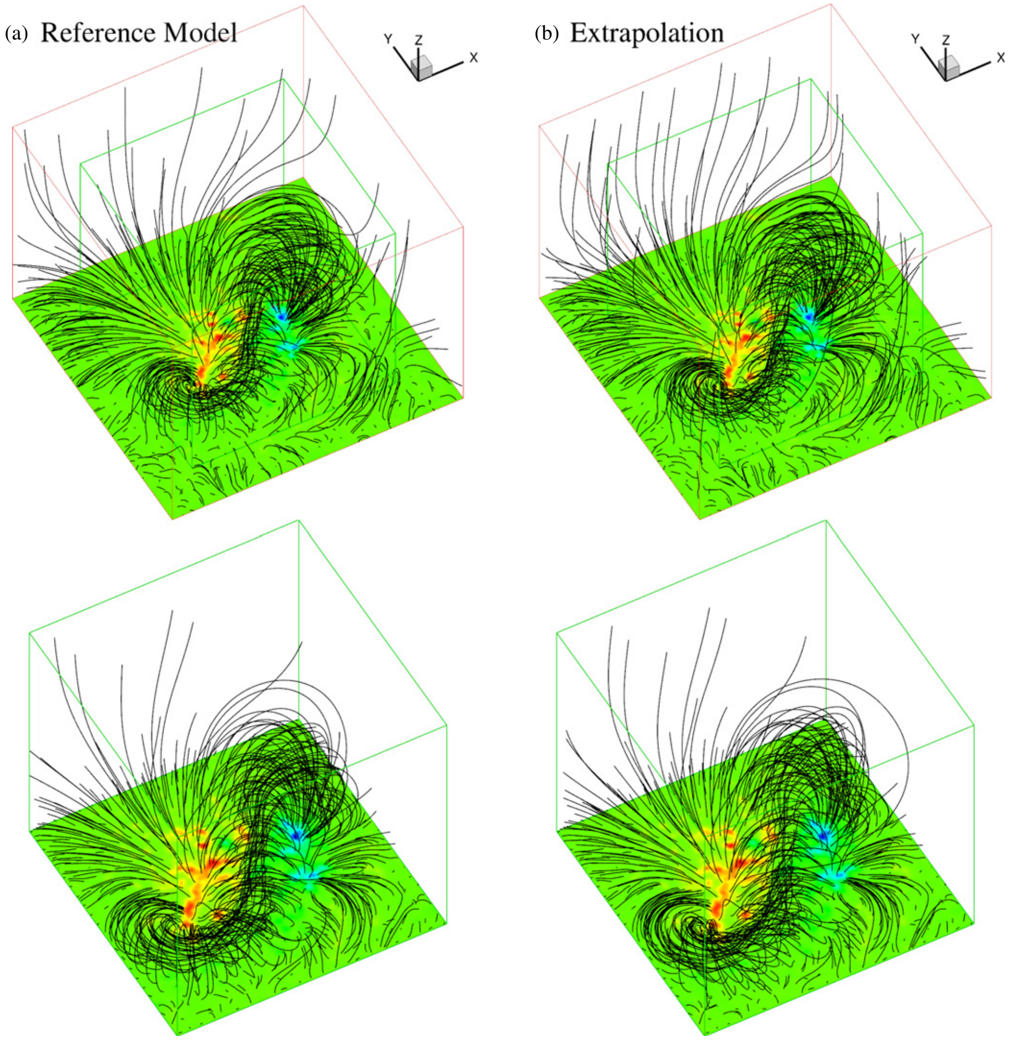
(a) Reference Model

(b) Extrapolation

Figure 10. Chromospheric test case of the van Ballegooijen reference model: magnetic field lines with a contour of B_z on the bottom surface. (a) The reference model, (b) the extrapolation result. The bottom row enlarges the central region outlined by the small cube in the top row.

(A color version of this figure is available in the online journal.)

Table 6
The van Ballegooijen Reference Model: Metrics of $E_{\nabla\times\mathbf{B}}$ and $E_{\nabla\cdot\mathbf{B}}$

Model	$E_{\nabla\times\mathbf{B}}$	$E_{\nabla\cdot\mathbf{B}}$
For $z \in [2, 225]$		
Reference	0.018	0.004
Our result of the chromospheric case	0.023	0.005
Our result of the photospheric case	0.048	0.015
For $z \in [2, 61]$		
Reference	0.060	0.010
Our result of the chromospheric case	0.072	0.014
Our result of the photospheric case	0.132	0.040

In Paper II, both cases with the raw and preprocessed photospheric magnetograms are tested, and it is found that the preprocessed case gives a significantly better result than the raw case in which the flux rope is not reproduced at all. This demonstrated that the preprocessing procedure is necessary for those extrapolation codes. Besides, the smoothing involved in the preprocessing also benefits the extrapolation code, which is based on a numerical finite difference.

Table 7
The van Ballegooijen Reference Model: Metrics for Extrapolation of the Photospheric Case

Model	C_{vec}	C_{CS}	E'_{n}	E'_{m}	E/E_{pot}	CWsin	$\langle\lvert f_i\rvert\rangle$
For $z \in [2, 225]$							
Reference	1.000	1.000	1.000	1.000	1.531	0.107	1.02×10^{-4}
Our result	0.970	0.968	0.783	0.679	1.146	0.257	2.29×10^{-4}
Wiegelmann*	0.98	0.97	0.77	0.65	1.18	0.26	
Wheatland*	0.88	0.96	0.69	0.65	1.03	0.11	
Potential	0.850	0.945	0.659	0.636	1.000		
For $z \in [2, 61]$							
Reference	1.000	1.000	1.000	1.000	1.559	0.103	1.33×10^{-4}
Our result	0.970	0.980	0.800	0.791	1.149	0.230	3.45×10^{-4}
Potential	0.845	0.891	0.629	0.646	1.000		

Note. The superscript "$*$" denotes the reported results in Table 3 of Paper II.

Our result is given in Figure 13 and Table 6. The field lines show that the overall structure, including the flux rope, is still recovered qualitatively, but only partially. By careful comparison with the reference or the chromospheric cases, the

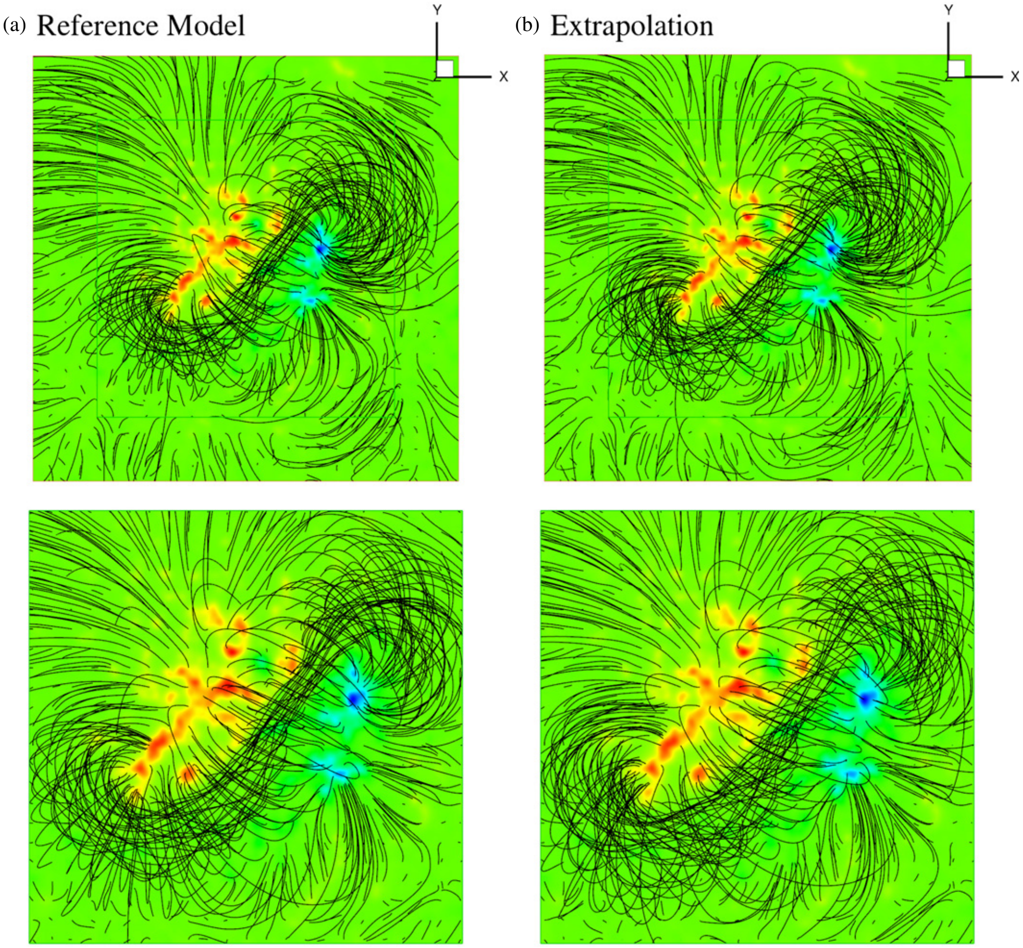
(a) Reference Model

(b) Extrapolation

Figure 11. Chromospheric test case of the van Ballegooijen reference model: same as Figure 10 but projected onto the *x*–*y* planes.

(A color version of this figure is available in the online journal.)

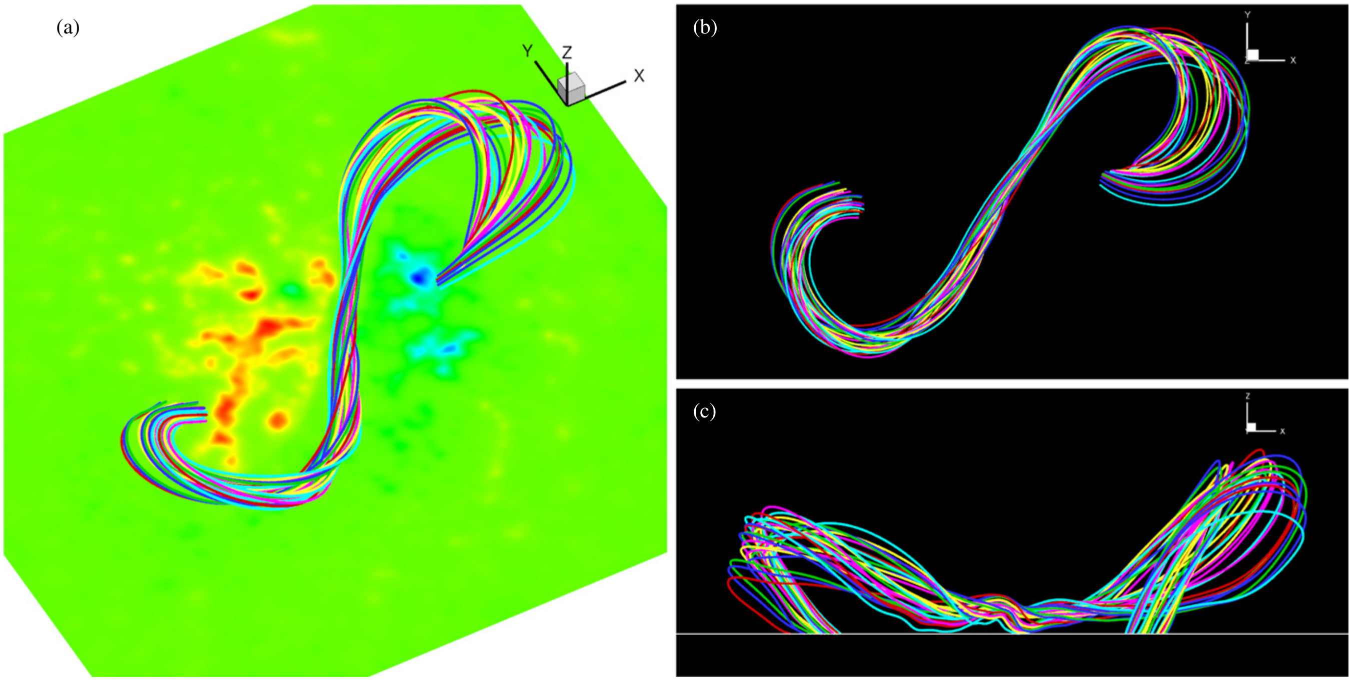

Figure 12. van Ballegooijen reference model: different views of the flux rope. (a) Three-dimensional view, (b) projection on the *x*–*y* plane, and (c) on the *x*–*z* plane with the white line denoting the bottom. Since the middle of the flux rope lies proximal to the bottom, the *z* scale in panel (c) is doubled for a better view of the field lines.

(A color version of this figure is available in the online journal.)

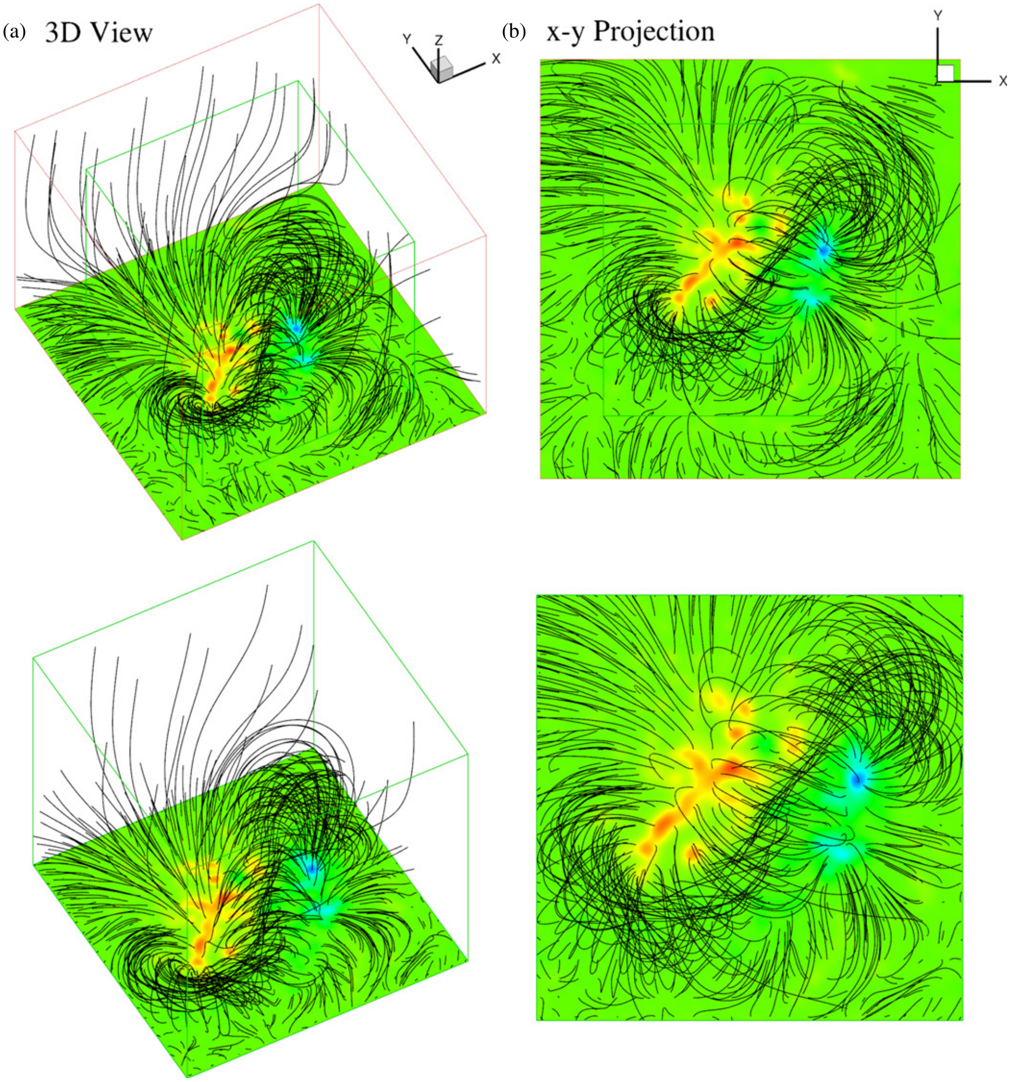

Figure 13. Photospheric test case of the van Ballegooijen reference model: magnetic field lines with contour of B_z on the bottom surface. (a) Three-dimensional (3D)view and (b) x–y plane projection of the extrapolation result. The bottom row enlarges the central region outlined by the small cube in the top row.

(A color version of this figure is available in the online journal.)

difference is also evident, e.g., the bundle of S-shaped lines is much thinner in the present case, which seems to suggest that many field lines have not fully reconnected to form an entire S. The quantitative comparison also demonstrates that the extrapolation quality is a bit worse than the chromospheric case, which can especially be seen in the CWsin and $E_{\nabla\times\mathbf{B}}$ metrics (nearly twice those of the chromospheric case). It means that the extrapolated field is farther away from the exactly force-free state than the chromospheric case. The free energy is also substantially underestimated much like the results in Paper II. This is because the preprocessing does not recover a force-free magnetogram that is entirely consistent with the reference model. Still, it is worthwhile noting that our result again reaches the same level of the best result in Paper II, and some of the metrics, including the most sensitive one $E_{\rm m}$, perform even better than Wiegelmann's.

6. CONCLUSIONS

As a viable way to study the magnetic field in the corona, the NLFFF extrapolation also needs considerable effort to be devoted to its numerical realization. In this paper, a new numerical implementation of NLFFF extrapolation is presented based on the MHD-relaxation method and the CESE-MHD code. Our implementation stands out because of the following aspects.

1. The magnetofrictional approach that is designed for speeding the relaxation of the MHD system (Roumeliotis 1996; Valori et al. 2007) is realized for the first time by the high-performance CESE scheme on a grid without any type of ghost zone or buffer layer.
2. The accuracy is further improved by first utilizing the magnetic splitting form (Tanaka 1994) for NLFFF methods to totally avoid the numerically random errors involved with the initial input.
3. Multimethod control, i.e., the diffusive and convection term, of numerical magnetic monopoles is employed for effectively reducing the divergence error.
4. The vector magnetogram is inputted at the bottom boundary in the way of time-linearly modifying the potential field to match the magnetogram, and other artificial boundaries are

fixed as initial potential values, making our implementation much easier than other MHD-relaxation methods (e.g., those by Roumeliotis 1996 and Valori et al. 2007).

5. The code is highly parallelized with the help of the PARAMESH toolkit and was performed on the share-memory parallel computer. It can be readily realized with the AMR technique and applied to a very high resolution magnetogram in the near future. The multigrid-type algorithm is also incorporated into the code to speed up the computation as recommended.

We have examined the capability of the method using several reference solutions of NLFFF that can serve as a suite of benchmark tests for any NLFFF extrapolation code. These test cases consist of the classic half-analytic force-free fields by Low & Lou (1990) and the much more stringent and solar-like reference solution by van Ballegooijen (2004). The results show that our method is successful and versatile for extrapolations of either the relatively simple cases or the rather complex cases that need significant rebuilding of the magnetic topology, e.g., the flux rope. We also compute a suite of metrics to quantitatively analyze the results and show that the solutions are extrapolated with high accuracies that are very close to, and even surpass, the best results by Wiegelmann (2004) after comparing the metrics. This demonstrated that, at least in computation accuracy, our code performs as well as the best state-of-the-art one (the computing time of the code, however, is difficult to compare because the hardwares are different). In addition, we introduced a pair of metrics for the assessment of the divergence-freeness and force-freeness of the extrapolation, $E_{\nabla\cdot\mathbf{B}}$ and $E_{\nabla\times\mathbf{B}}$, which further demonstrated that our code can fulfill the solenoidal constraint well and minimize the Lorentz force to the same level of the reference values.

The success of our implementation encouraged us that, with a good solver, the MHD-relaxation approach can also extrapolate the NLFFF as accurately as other good-performance algorithms such as the weighting optimization method. This confirms again that the implementation of the method plays the same important role as the underlying approach. It is especially worthwhile to point out that, as also noted by Wiegelmann (2008), the MHD-relaxation approach has a great advantage over other methods: any available time-dependent MHD code can be adjusted for NLFFF extrapolations, thus saving major effort that should be used instead to develop a new code from scratch for a special method. We are also inspired by Valori et al. (2007), who show that a higher order scheme can significantly advance the extrapolation. In our project, an arbitrary high-order CESE scheme is under development and is expected to be used to improve our implementation in the future.

Recently, more critical tests of extrapolation codes have been performed by Schrijver et al. (2008) and DeRosa et al. (2009) based on vector magnetograms of AR 10930 and 10953 from the *Hinode* Solar Optical Telescope and observed coronal loops. It was found that the Grad–Rubin-style current-field iteration implemented by Wheatland (2006) surpassed the Wiegelmann's (2004) code, which performs best in the benchmark tests, and basically results from different methods are very inconsistent with each other. This shows that the idealized tests are unable to assess the code's ability to handle various uncertainties or errors in real magnetograms, and a more critical assessment of the code using realistic vector magnetograms is also planned in our future work.

The present extrapolation in Cartesian geometry is often limited to relatively local areas, e.g., a single active region without any relationship with others. However, the active regions cannot be isolated since they generally interact with neighboring ARs or overlaying large-scale fields. It should also be pointed out that the fields of view in a Cartesian box are often too small to properly characterize the entire relevant current system (DeRosa et al. 2009). To study the connectivity between multiactive regions and extrapolate in a larger field of view, it is necessary to take into account the curvature of the Sun's surface by extrapolating in spherical geometry partly or even entirely, i.e., including the global corona (Wiegelmann 2007; Tadesse et al. 2011, 2012). Moreover, a global NLFFF extrapolation could also avoid any lateral artificial boundaries, which are inescapable and cause issues in Cartesian codes. We are now on the path to develop a global NLFFF code for the new era of routine observation of the global vector magnetogram (which will be opened by the Helioseismic and Magnetic Imager on board *SDO*). Recently, during a project of constructing a data-driven MHD model for the global coronal evolution, we established the CESE method on a so-called Yin–Yang overlapping grid in spherical geometry (Kageyama & Sato 2004). This implementation, combined with our present NLFFF code, will make the realization of a global NLFFF extrapolation viable if provided with the global vector magnetogram. The Yin–Yang grid is composed of two identical component grids that are combined in a complementary way to cover an entire spherical surface with partial overlap of their boundaries. Each component grid is a low-latitude part of the latitude–longitude grid without the pole, and hence the grid spacing on the sphere surface is quasi-uniform. In this way, we can avoid the problem of grid convergence or grid singularity at both poles, which will otherwise arise if an entire spherical-coordinate grid is used, as Wiegelmann (2007) has pointed out. However, up to now, there is no suitable test case used for the global NLFFF extrapolation other than the simple axially symmetric Low & Lou cases. Most recently, Contopoulos et al. (2011) give a variety of global near-force-free solutions by a force-free electrodynamics code, solely using the radial magnetogram. Their solutions, however, are not unique to the same radial magnetogram; instead, they depend on the initial conditions and on the particular approach to the steady state.[1] Anyway, we believe their solutions can be used as much more realistic and solar-like tests for global NLFFF codes than the semianalytic solutions. In our future work, we will develop and test a new global NLFFF code using the global force-free solutions from Contopoulos et al. (2011).

This work is jointly supported by the National Natural Science Foundation of China (41031066, 40921063, 40890162, and 41074122), the 973 project under grant 2012CB825601, and the Specialized Research Fund for State Key Laboratories. We are grateful to Dr. Marc Derosa for providing the data of the van Ballegooijen reference model. The PARAMESH software used in this work was developed at the NASA Goddard Space Flight Center and Drexel University under NASA's HPCC and ESTO/CT Projects and under grant NNG04GP79G from the NASA/AISR project.

---

[1] They are also improving their code to make use of the vector magnetogram to uniquely define the solutions (I. Contopoulos & C. Kalapotharakos 2011, private communication).

APPENDIX A

THE SPECIFIC FORM OF EQUATION (11)

$$\mathbf{F} = \begin{pmatrix} \mathbf{B}_1 \cdot \mathbf{B}_1/2 - B_{1x}^2 - (B_{0x}B_{1x} + B_{1x}B_{0x}) + \mathbf{B}_0 \cdot \mathbf{B}_1 \\ -B_{1x}B_{1y} - (B_{0x}B_{1y} + B_{1x}B_{0y}) \\ -B_{1x}B_{1z} - (B_{0x}B_{1z} + B_{1x}B_{0z}) \\ 0 \\ v_xB_y - v_yB_x \\ v_xB_z - v_zB_x \\ 0 \\ 0 \\ 0 \end{pmatrix};$$

$$\mathbf{G} = \begin{pmatrix} -B_{1y}B_{1x} - (B_{0y}B_{1x} + B_{1y}B_{0x}) \\ \mathbf{B}_1 \cdot \mathbf{B}_1/2 - B_{1y}^2 - (B_{0y}B_{1y} + B_{1y}B_{0y}) + \mathbf{B}_0 \cdot \mathbf{B}_1 \\ -B_{1y}B_{1z} - (B_{0y}B_{1z} + B_{1y}B_{0z}) \\ v_yB_x - v_xB_y \\ 0 \\ v_yB_z - v_zB_y \\ 0 \\ 0 \\ 0 \end{pmatrix};$$

$$\mathbf{H} = \begin{pmatrix} -B_{1z}B_{1x} - (B_{0z}B_{1x} + B_{1z}B_{0x}) \\ -B_{1z}B_{1y} - (B_{0z}B_{1y} + B_{1z}B_{0y}) \\ \mathbf{B}_1 \cdot \mathbf{B}_1/2 - B_{1z}^2 - (B_{0z}B_{1z} + B_{1z}B_{0z}) + \mathbf{B}_0 \cdot \mathbf{B}_1 \\ v_zB_x - v_xB_z \\ v_zB_y - v_yB_z \\ 0 \\ 0 \\ 0 \\ 0 \end{pmatrix}; \tag{A1}$$

$$\begin{aligned} \mathbf{F}_\nu &= (0, 0, 0, \mu\nabla \cdot \mathbf{B}_1, 0, 0, 0, 0, 0)^T; \\ \mathbf{G}_\nu &= (0, 0, 0, 0, \mu\nabla \cdot \mathbf{B}_1, 0, 0, 0, 0)^T; \\ \mathbf{H}_\nu &= (0, 0, 0, 0, 0, \mu\nabla \cdot \mathbf{B}_1, 0, 0, 0)^T; \end{aligned} \tag{A2}$$

and

$$\mathbf{S} = (-\nu\rho v_x, -\nu\rho v_y, -\nu\rho v_z, v_x\nabla\cdot\mathbf{B}_1, v_y\nabla\cdot\mathbf{B}_1, v_z\nabla\cdot\mathbf{B}_1, 0, 0, 0). \tag{A3}$$

REFERENCES

Abbett, W. P., & Fisher, G. H. 2003, ApJ, 582, 475

Abbett, W. P., Mikić, Z., Linker, J. A., et al. 2004, J. Atmos. Sol.-Terr. Phys., 66, 1257

Altschuler, M. D., & Newkirk, G. 1969, Sol. Phys., 9, 131

Aly, J. J. 1989, Sol. Phys., 120, 19

Amari, T., Aly, J. J., Luciani, J. F., Boulmezaoud, T. Z., & Mikic, Z. 1997, Sol. Phys., 174, 129

Amari, T., Boulmezaoud, T. Z., & Aly, J. J. 2006, A&A, 446, 691

Amari, T., Boulmezaoud, T. Z., & Mikic, Z. 1999, A&A, 350, 1051

Aschwanden, M. J. (ed.) 2005, Physics of the Solar Corona, An Introduction with Problems and Solutions (2nd ed.; New York: Springer)

Canou, A., & Amari, T. 2010, ApJ, 715, 1566

Chang, S. C. 2002, Proc. 38th AIAA Joint Propulsion Conf., Indianapolis, IN, AIAA-2002-3890, www.grc.nasa.gov/WWW/microbus/cese/PUBS/aiaa2002-3890.pdf

Chodura, R., & Schlueter, A. 1981, J. Comput. Phys., 41, 68

Contopoulos, I., Kalapotharakos, C., & Georgoulis, M. K. 2011, Sol. Phys., 269, 351

Dedner, A., Kemm, F., Kröner, D., et al. 2002, J. Comput. Phys., 175, 645

Dellar, P. J. 2001, J. Comput. Phys., 172, 392

DeRosa, M. L., Schrijver, C. J., Barnes, G., et al. 2009, ApJ, 696, 1780

Feng, X., Hu, Y., & Wei, F. 2006, Sol. Phys., 235, 235

Feng, X. S., Yang, L. P., Xiang, C. Q., et al. 2010, ApJ, 723, 300

Feng, X., Zhou, Y., & Wu, S. T. 2007, ApJ, 655, 1110

Grad, H., & Rubin, H. 1958, in 2nd Int. Conf. Peac. Uses of Atom. Energy, Vol. 31 (Geneva: UN), 190

Hayashi, K. 2005, ApJS, 161, 480

He, H., & Wang, H. 2008, J. Geophys. Res., 113, 5

He, H., Wang, H., & Yan, Y. 2011, J. Geophys. Res., 116, 1101

Hoeksema, J. T. 1984, PhD thesis, Stanford Univ., CA

Inhester, B., & Wiegelmann, T. 2006, Sol. Phys., 235, 201

Inoue, S., Kusano, K., Magara, T., Shiota, D., & Yamamoto, T. T. 2011, ApJ, 738, 161

Jiang, C. W., Cui, S. X., & Feng, X. S. 2012, Comput. Fluids, 54, 105

Jiang, C. W., Feng, X. S., Fan, Y. L., & Xiang, C. Q. 2011, ApJ, 727, 101

Jiang, C. W., Feng, X. S., Zhang, J., & Zhong, D. K. 2010, Sol. Phys., 267, 463

Kageyama, A., & Sato, T. 2004, Geochem. Geophys. Geosyst., 5, 9005

Linker, J. A., Mikić, Z., Biesecker, D. A., et al. 1999, J. Geophys. Res., 104, 9809

Low, B. C., & Lou, Y. Q. 1990, ApJ, 352, 343

MacNeice, P., Olson, K. M., Mobarry, C., de Fainchtein, R., & Packer, C. 2000, Comput. Phys. Commun., 126, 330

Marder, B. 1987, J. Comput. Phys., 68, 48

McClymont, A. N., Jiao, L., & Mikic, Z. 1997, Sol. Phys., 174, 191

Metcalf, T. R., DeRosa, M. L., Schrijver, C. J., et al. 2008, Sol. Phys., 247, 269

Mikić, Z., Linker, J. A., Schnack, D. D., Lionello, R., & Tarditi, A. 1999, Phys. Plasmas, 6, 2217

Mikic, Z., & McClymont, A. N. 1994, in ASP Conf. Ser. 68, Solar Active Region Evolution: Comparing Models with Observations, ed. K. S. Balasubramaniam & G. W. Simon (San Francisco, CA: ASP), 225

Nakagawa, Y. 1974, ApJ, 190, 437

Nakamizo, A., Tanaka, T., Kubo, Y., et al. 2009, J. Geophys. Res.(Space Phys.), 114, A07109

Powell, K. G., Roe, P. L., Linde, T. J., Gombosi, T. I., & de Zeeuw, D. L. 1999, J. Comput. Phys., 154, 284

Roumeliotis, G. 1996, ApJ, 473, 1095

Sakurai, T. 1981, Sol. Phys., 69, 343

Sakurai, T. 1989, Space Sci. Rev., 51, 11

Schrijver, C. J., De Rosa, M. L., Metcalf, T. R., et al. 2006, Sol. Phys., 235, 161

Schrijver, C. J., De Rosa, M. L., Metcalf, T., et al. 2008, ApJ, 675, 1637

Song, M. T., Fang, C., Tang, Y. H., Wu, S. T., & Zhang, Y. A. 2006, ApJ, 649, 1084

Tadesse, T., Wiegelmann, T., Inhester, B., & Pevtsov, A. 2011, A&A, 527, A30

Tadesse, T., Wiegelmann, T., Inhester, B., & Pevtsov, A. 2012, Sol. Phys., 277, 119

Tanaka, T. 1994, J. Comput. Phys., 111, 381

Tóth, G., & Roe, P. L. 2002, J. Comput. Phys., 180, 736

Valori, G., Kliem, B., & Fuhrmann, M. 2007, Sol. Phys., 245, 263

Valori, G., Kliem, B., & Keppens, R. 2005, A&A, 433, 335

van Ballegooijen, A. A. 2004, ApJ, 612, 519

van Ballegooijen, A. A., Deluca, E. E., Squires, K., & Mackay, D. H. 2007, J. Atmos. Sol.-Terr. Phys., 69, 24

van Ballegooijen, A. A., Priest, E. R., & Mackay, D. H. 2000, ApJ, 539, 983

Wang, A. H., Wu, S. T., Tandberg-Hanssen, E., & Hill, F. 2011, ApJ, 732, 19

Welsch, B. T., Fisher, G. H., Abbett, W. P., & Regnier, S. 2004, ApJ, 610, 1148

Wheatland, M. S. 2004, Sol. Phys., 222, 247

Wheatland, M. S. 2006, Sol. Phys., 238, 29

Wheatland, M. S., Sturrock, P. A., & Roumeliotis, G. 2000, ApJ, 540, 1150

Wiegelmann, T. 2004, Sol. Phys., 219, 87

Wiegelmann, T. 2007, Sol. Phys., 240, 227

Wiegelmann, T. 2008, J. Geophys. Res., 113, 3

Wiegelmann, T., & Neukirch, T. 2006, A&A, 457, 1053

Wu, S. T., Sun, M. T., Chang, H. M., Hagyard, M. J., & Gary, G. A. 1990, ApJ, 362, 698

Wu, S. T., Wang, A. H., Gary, G. A., et al. 2009, Adv. Space Res., 44, 46

Wu, S. T., Wang, A. H., Liu, Y., & Hoeksema, J. T. 2006, ApJ, 652, 800

Wu, S. T., Zheng, H., Wang, S., et al. 2001, J. Geophys. Res., 106, 25089

Yang, W. H., Sturrock, P. A., & Antiochos, S. K. 1986, ApJ, 309, 383

Yan, Y., & Li, Z. 2006, ApJ, 638, 1162

Yan, Y., & Sakurai, T. 2000, Sol. Phys., 195, 89

Zhang, M., John Yu, S., Henry Lin, S., Chang, S., & Blankson, I. 2006, J. Comput. Phys., 214, 599